

Mesoscale variability in the Arabian Sea

P. L'Hégaret et al.

Mesoscale variability in the Arabian Sea from HYCOM model results and observations: impact on the Persian Gulf Water path

P. L'Hégaret¹, R. Duarte², X. Carton¹, C. Vic¹, D. Ciani¹, R. Baraille³, and S. Corréard³

¹LPO, UBO/UEB and IFREMER, Brest, France

²ACTIMAR, Brest, France

³SHOM, Toulouse, France

Received: 5 January 2015 – Accepted: 18 February 2015 – Published: 12 March 2015

Correspondence to: P. L'Hégaret (pierre.lhegaret@univ-brest.fr)

Published by Copernicus Publications on behalf of the European Geosciences Union.

Title Page

Abstract

Introduction

Conclusions

References

Tables

Figures



Back

Close

Full Screen / Esc

Printer-friendly Version

Interactive Discussion



Abstract

The Arabian Sea and Sea of Oman circulation and water masses, subject to the monsoon forcing, reveal a strong seasonal variability and intense mesoscale features. We describe and analyse this variability and these features, using both meteorological data (from ECMWF reanalyses), in-situ observations (from the ARGO float program and the GDEM climatology), satellite altimetry (from AVISO) and a regional simulation with a primitive equation model (HYCOM). The EOFs of the seasonal variability of the water masses quantify their main changes in thermohaline characteristics and in position. The model and observations display comparable variability, and the model is then used to analyse the three-dimensional structure of eddies and water masses with a higher resolution. The mesoscale eddies have a deep dynamical influence and strongly drive the water masses at depth. In particular, in the Sea of Oman, the Persian Gulf Water presents several offshore ejection sites and a complex recirculation, depending on the mesoscale eddies. This water mass is also captured inside the eddies via several mechanisms, keeping high thermohaline characteristics in the Arabian Sea. These characteristics are validated on the GOGP99 cruise data.

1 Introduction

The circulation and water masses in the Northern Arabian Sea and the Sea, or Gulf, of Oman are investigated here using a numerical ocean model at mesoscale resolving resolution, in-situ and remote sensing data. The focus lies on the seasonal structure and variability of intense mesoscale features and on their impact on the outflow of Persian Gulf Water (hereafter PGW).

The ocean circulation in the Arabian Sea is characterized by a strong seasonal variability related to the reversal of the monsoon wind direction and to the changes in atmospheric fluxes. During the winter monsoon (from November to February) winds blow from the North-East over the Arabian Sea and during the summer monsoon (from

OSD

12, 493–550, 2015

Mesoscale variability in the Arabian Sea

P. L'Hégaret et al.

Title Page

Abstract

Introduction

Conclusions

References

Tables

Figures

◀

▶

◀

▶

Back

Close

Full Screen / Esc

Printer-friendly Version

Interactive Discussion



Mesoscale variability in the Arabian Sea

P. L'Hégaret et al.

Title Page

Abstract

Introduction

Conclusions

References

Tables

Figures



Back

Close

Full Screen / Esc

Printer-friendly Version

Interactive Discussion



June to September), stronger winds blow from the South-West. The monsoons are interleaved by short transition periods in spring and fall when winds are weaker and variable in direction (see Defant, 1961).

Due to the strong winds, several seasonal upwellings occur in the coastal regions (see Shi et al., 2000). The most noticeable is the upwelling near the Somalia, Yemen and Oman coasts during the summer monsoon with the production of very long cold filaments protruding from the coast.

The whole region is characterized by a high annual evaporation rate and the net E-P budget is very large and positive in the Persian Gulf and in the Red Sea. This leads to the generation of water masses with very high salinities (above 40 psu) in these two basins (see Yao and Johns, 2010a, b; Bower et al., 2000).

The Persian Gulf is a very shallow sea with an average depth of about 35 m and maximum depths around 100 m. Very salty and dense water, Persian Gulf Water, is formed on the western boundary of the Persian Gulf via evaporation. This water flows through the Strait of Hormuz and spreads in the Sea of Oman and in the Arabian Sea (see Bower et al., 2000 and Fig. 1 for locations and bathymetry). Observations show that the annual mean outflow transport of PGW through the strait is about 0.25 Sv, with few seasonal variations in transport (see Matsuyama et al., 1998; Johns et al., 2000). It has been shown that this transport can be affected by short-term pulses, which were related to the effect of oceanic cyclones in the Persian Gulf (see Thoppil and Hogan, 2009). Outflowing PGW is colder and saltier in winter (Pous et al., 2004a).

In the northern part of the Sea of Oman, PGW reaches an equilibrium depth between 150 and 250 m. The PGW plume tends to deepen away from the straits. It can be found at 250–350 m depth South of the Arabian peninsula (see Bower et al., 2000; Pous et al., 2004b; Carton et al., 2012).

Seasonal or higher frequency variability of the surface circulation in the Sea of Oman has already been evidenced and related to atmospheric forcing (seasonal wind stress or the effect of atmospheric cyclones) and to Rossby waves issued from the eastern boundary (Pakistan and India, see Schott et al., 2009). In particular, mesoscale oceanic

dipoles (cyclone+anticyclone), as well as isolated eddies, have been observed in the vicinity of Ra's al Hamra (see L'Hégaret et al., 2013) and Ra's al Hadd (see Wang et al., 2013).

Due to these perturbations (irregularity in the outflow transport and presence of mesoscale eddies, as well as topographic accidents), the PGW outflow is expected to be disrupted and to shed fragments. Indeed, this was observed: PGW can form patches and recirculate in the Sea of Oman. More prominently, a mesoscale, intrathermocline eddy of PGW was once observed near the straits, extending towards the middle of the Sea of Oman (see Senjyu et al., 1998; L'Hégaret et al., 2013).

The objective of this paper is twofold. First, we investigate and rationalize the mesoscale variability in the Sea of Oman and Arabian Sea, to characterize its three-dimensional structure, and its seasonal variability. Second, we determine the various modes of detachment of PGW fragments from the plume, in particular due to these mesoscale structures. To achieve this purpose, a primitive equation model is implemented regionally and the results of the simulations are analyzed in conjunction with synoptic in situ and surface data.

The paper is organized as follows: the model characteristics and the origin and nature of data are first specified; the regional structure and seasonal variability of the water masses and currents in the region are then described from the two independent data sources; the mesoscale structures and their interactions are characterized and finally, the impact of these structures on the PGW outflow is quantified.

2 Model and data

The numerical simulations were performed with the Hybrid Coordinate Ocean Model (HYCOM) (see Chassignet et al., 2007). HYCOM is a primitive equation, hybrid coordinate model (isopycnal and z). The model variables are discretized on a horizontal Arakawa C-grid. The horizontal resolution is here 5 km and the model has 40 vertical levels. The simulation is initiated with a state given by a lower resolution global

Mesoscale variability in the Arabian Sea

P. L'Hégaret et al.

Title Page

Abstract

Introduction

Conclusions

References

Tables

Figures



Back

Close

Full Screen / Esc

Printer-friendly Version

Interactive Discussion



Mesoscale variability in the Arabian Sea

P. L'Hégaret et al.

Title Page

Abstract

Introduction

Conclusions

References

Tables

Figures



Back

Close

Full Screen / Esc

Printer-friendly Version

Interactive Discussion



model (MERCATOR) and it is forced by realistic atmospheric fields (from the French Met'Office METEO FRANCE) cycling over 2011. The tidal forcing is provided by Topex and is included as a boundary condition. We produced a 11 year simulation starting in 2011. The first five years correspond to the spin-up of the model and were discarded.

The spin-up was considered achieved when the mesoscale circulation was well established and the properties of the main water masses reached their typical values. Only the last six years of the simulation were analyzed; in our timeline, they are noted 2016 to 2021.

To study the thermohaline variability over the season we used a modified GDEM (Generalized Digital Environmental Model) climatology. GDEM is a monthly climatology constructed from MOODS (Master Oceanographic Observational Data Set) profiles, with 72 vertical levels and a $1/4^\circ \times 1/4^\circ$ horizontal resolution (see Carnes, 2009 for climatology construction). This climatology provided the better results for the Arabian Sea and the bordering gulfs and seas. To improve the horizontal resolution and to follow the different water masses we added profiles from ARGO floats. These long lived drifters provide high quality profiles for temperature and salinity. We used the ANDRO dataset for floats released before 2010 and the CORIOLIS (France) and INCOIS (India) database for later ones. Over 100 floats were found to be drifting North of 18° N in the Arabian Sea between 2002 and 2014 which corresponds to 550 to 600 profiles per month, on average.

The surface fluxes were issued from a monthly meteorological model reanalysis by ECMWF. This provided monthly climatologies of wind, heat, evaporation and precipitation fluxes over 40 years with a resolution of 0.7° . The horizontal resolution is low but sufficient to resolve the mesoscale, and provided a dataset on a long period of time, necessary to compute climatology. Nevertheless, the calculation of derivatives, as the wind stress can still present strong horizontal gradients. We also used altimetric data from AVISO over 22 years, from 1992 to 2014. From the ADT (Altimetric Dynamic Topography), the instantaneous spatial average was subtracted, to obtain "ADT anomalies".

Empirical Orthogonal Function's (EOF) were also calculated from the horizontal fields to determine the spatial and temporal variability of the oceanic variables.

3 Regional features and model validation

3.1 Wind forcing

5 Atmospheric and oceanic processes in the Arabian Sea and Sea of Oman are strongly constrained by the monsoonal cycle. Here we determined the transitions in wind stress curl North of 18° N which outline two strong regimes that last 4 months, in summer and winter, and two regimes of transition, the inter monsoons, in spring and autumn that last respectively three and one months. The seasonal variability of the wind forcing is described in Appendix A. We focus here on the wind stress curl $\mathbf{k} \cdot \nabla \wedge \boldsymbol{\tau}$ with $\boldsymbol{\tau} = \rho_{\text{air}} C_d$ $\|\mathbf{U}\| \mathbf{U}$, with ρ_{air} the air density, \mathbf{U} the wind speed at 10 m a.s.l. and C_d a drag coefficient of about 1×10^{-3} , varying with the wind speed (see Kumar et al., 2009). Figure 2 shows the averaged wind stress and wind stress curl respectively over a $2^\circ \times 2^\circ$ square off coast, East of Ra's Al Hadd. These graphs allow us to choose four characteristic months to study the mesoscale dynamics. July and December have the strongest wind stress for each monsoon season and are, respectively, a minimum and a maximum in the wind stress curl. October and March have the lowest wind stress and opposite sign. The wind stress curl graph (see Fig. 2, right) shows that these months are a transition period from one monsoon to another.

20 In summer, the monsoonal wind orientation induces a net Ekman transport (see Fig. 3) offshore from most coasts (Yemen, Oman, Iran, Pakistan), except from the coast of India to which it is parallel. This leads to the formation of upwellings and to a negative sea level anomaly where a coastal geostrophically balanced current sits.

25 In fall, the wind loses its intensity and orientation, subsequently the Ekman transport and its related effects are reduced.

**Mesoscale variability
in the Arabian Sea**

P. L'Hégaret et al.

Title Page

Abstract

Introduction

Conclusions

References

Tables

Figures



Back

Close

Full Screen / Esc

Printer-friendly Version

Interactive Discussion



the contrast. This contrast is related to the offshore or onshore Ekman transport and pumping in the interior of the basin as mentioned above. On the first EOF from HYCOM this contrast between the coastal signatures and the interior of the basin is also present. Anomalies with the same sign of the coastal ones are found near the mouth of the Sea of Oman and along 20° N. The time serie of the amplitude from HYCOM is similar to AVISO's.

The second EOF from AVISO shows the presence of intense eddies offshore of Ra's Al Hadd. This situation occurs essentially during the spring and fall intermonsoons with reverse amplitudes. As the strong winds decay, the forced circulation relaxes and EKE is found to peak there (see Vic et al., 2014). For HYCOM, the second EOF appears as a composite of the first and second EOF from AVISO, with a sign difference between the coastal and the inner basin anomalies, but with more mesoscale structures. The time series also indicate that this situation occurs preferentially in fall and spring, in phase with EKE peaks.

The third EOF also shows the presence of eddies along Arabian Peninsula with a stronger amplitude at the end of each season. On AVISO the positive anomaly in the Gulf of Khambhat is due to tides and rivers outflow.

On all three EOF's, eddies lie off the southern coast of Oman with a strong amplitude in spring and in fall. Therefore, they must be long lasting and recurrent (from year to year). Their origin is investigated in the following section.

3.3 Water masses and thermohaline forcings

With two strong evaporation basins, the Red Sea and the Persian Gulf, and a region of colder and fresher water masses, the neighbouring Bay of Bengal with atmospheric forcing bringing upwellings and downwellings, strong evaporation and precipitation fluxes, numerous water masses can be found in the Arabian Sea. Here we focus on two regions, the northern Arabian Sea, North of 15° N, and the Sea of Oman, without the Strait of Hormuz. In situ measurements with ARGO floats are compared to the output of the HYCOM model.

Mesoscale variability in the Arabian Sea

P. L'Hégaret et al.

Title Page

Abstract

Introduction

Conclusions

References

Tables

Figures



Back

Close

Full Screen / Esc

Printer-friendly Version

Interactive Discussion



In the northern Arabian Sea (see Fig. 5) a striking difference between the model and the in situ data can be easily observed. Several profiles present fresher water and a constant temperature of about 30 °C that crosses isopycnals. This corresponds to the river input that spreads along the Indian coast on the continental shelf, particularly through the Gulf of Khambhat, with the rivers Narmada, Tapti and Mahi with a transport of 2.3×10^{-3} Sv. Those waters are not measured by the ARGO floats which stay away from the shelf because of their parking depth, generally 1000 m. Figure 1 shows the positions of the ARGO profiles, with a lack of measurements along the Indian shelf. Furthermore, another light water, the Bay of Bengal water, with $\sigma_t = 22$ and low values of salinity is poorly sampled by the floats since its spreading mainly stays confined along the coast of India (see Kumar and Prasad, 2012). Despite those differences, other water masses can be found on both in situ data and model results. The main core of the profiles is the Indian Ocean Central Water, which presents relatively fresh and cold water, spreading along the isopycnal $\sigma_t = 25.5$. The Arabian Sea High Salinity Water can be found near the surface with strong salinity and σ_t varying from 22.8 in winter to 24.5 in late summer. The Persian Gulf Water peaks with high salinity, above 37 psu all year long with a density σ_t varying from 26.3 to 27. In the model the Persian Gulf Water is observed with a lighter density, around 26. The Red Sea Water, with σ_t of 27 is not found either in the ARGO measurements nor in the model, due to the focus zone being too far North from the region of advection.

The Sea of Oman (see Fig. 6) contains the Persian Gulf Water. The main differences between the in situ data and the model being the stronger salinities that are found in the northwestern part of the basin and not being sampled by the floats. This allows us to use the model to follow the spreading of the Persian Gulf Water, keeping in mind the difference of PGW density between the model and observations.

4 Mesoscale eddies formation and evolution

4.1 Formation

We now investigate the formation of the mesoscale structures. These coastal eddies originate from the coastal current, associated with the strip of negative MADT anomaly along Oman, Iran and Pakistan. This strip intensifies until August and forms meanders, then cyclonic eddies first (in summer, anticyclonic in winter) along the Iranian coast, then along the Omani coast (this can be seen when viewing time series of altimetry Fig. 7). The monsoon seasons are periods of intense formation of eddies along the coasts, mainly the western and northern ones. Due to a plateau near the coast of India, the formation occurs at 150 km offshore.

This current is fairly wide ($L \approx 150$ km) on altimetric maps and the associated geostrophic velocity is about $U_h = 0.25 \text{ m s}^{-1}$. We can estimate the likeliness of its barotropic instability by comparing U_h/L^2 and $\beta\sqrt{2}/2$ (to take into account the orientation of the southern coast of Arabia). The first term is on the order of $1.1 \times 10^{-11} \text{ m}^{-1} \text{ s}^{-1}$ and the second one is about $1.4 \times 10^{-11} \text{ m}^{-1} \text{ s}^{-1}$. The Rayleigh Kuo criterion for barotropic instability can thus be satisfied in order of magnitude.

We can also assess the possibility of baroclinic instability for this current. Using a simple two-layer Phillips model of baroclinic instability, with two equally thick layers and opposite surface and deep flows (see Vallis, 2006), the condition for existence of baroclinic instability is that the vertical shear of horizontal velocity U_s be larger than $\beta R_d^2/4$. Here R_d is about 40 km and the threshold is about 0.01 m s^{-1} . Taking $U_s = 2U_h = 0.5 \text{ m s}^{-1}$, baroclinic instability is also possible.

Maximum baroclinic instability is obtained under such conditions for $\lambda = 2\pi R_d/1.8 \approx 140$ km (theoretical value for a large shear), the half of which is comparable with the largest western eddy diameters in observations (approximately 200 km). Note that a similar estimate is obtained with the Eady model, $\lambda \approx 4R_d$, corresponding to a most unstable wavelength of 160 km (see also Smith, 2007).

Title Page

Abstract

Introduction

Conclusions

References

Tables

Figures

◀

▶

◀

▶

Back

Close

Full Screen / Esc

Printer-friendly Version

Interactive Discussion



Mesoscale variability in the Arabian Sea

P. L'Hégaret et al.

Title Page

Abstract

Introduction

Conclusions

References

Tables

Figures

◀

▶

◀

▶

Back

Close

Full Screen / Esc

Printer-friendly Version

Interactive Discussion



Finally the growth rate of these such unstable waves is $\sigma = 0.3U_s/R_d$ in the Phillips model, or about 1/10 days. The Eady model gives the same expression and result. On altimetric maps, it can be seen that eddies are fully formed within 4–6 weeks after the appearance of the meanders. This duration is about $3\sigma^{-1}$ (or 3 linear periods of instability), which takes into account the time necessary for wave growth and nonlinear interactions. Such a duration was commonly observed for eddy formation and detachment from an unstable jet, in previous studies of baroclinic instability (see Flierl et al., 1999).

Another possibility for the generation of these eddies is a localized, steady and strong wind stress curl forcing. This occurs in particular in the Sea of Oman and along the western coast of the basin, for all the seasons, and furthermore along the Indian coast in summer. The wind induced relative vorticity, expressed as $\Delta\xi = \frac{k \cdot \nabla \wedge \tau}{\rho_0 H} \Delta t$ (see Dong et al., 2007). We used here $\Delta t = 24$ h to keep the short period variations of the winds. We obtained a relative vorticity essentially negative over the basin with an exception in summer, with strong positive values North of Ra's Al Hadd, along the coast of Oman and the coast of India (South of 24° N). Moreover, the strongest values are found near these coasts and in the Sea of Oman with an order of magnitude of $2.5 \times 10^{-6} \text{ s}^{-1}$, positive in summer, negative the rest of the year. Comparatively this is about 35 % of the relative vorticity calculated from the sea surface height with $7 \times 10^{-6} \text{ s}^{-1}$ for the mesoscale eddies. As shown in L'Hégaret et al. (2013), in spring to early summer near Ra's al Hadd, the wind veers clockwise at this period and imparts anticyclonic vorticity to the ocean, thus reinforcing an anticyclonic eddy. A further amplification of this vorticity was then interpreted by the same authors as the result of the interaction with an incoming upwelling Rossby wave; this process will be studied in more detail here.

Time vs. longitude diagrams of the MADT anomaly from AVISO (Fig. 8) reveal two preferential bands of latitude with westward propagation of anomalies 21.5 and 24° N. Some of these anomalies have been identified as Rossby waves (see L'Hégaret et al., 2013) with wave speed of $c = -\beta R_d^2$ of 21 cm s^{-1} and with wavelength of about 150 km.

Mesoscale variability in the Arabian Sea

P. L'Hégaret et al.

Title Page

Abstract

Introduction

Conclusions

References

Tables

Figures

◀

▶

◀

▶

Back

Close

Full Screen / Esc

Printer-friendly Version

Interactive Discussion



These waves have also been observed more South by Heffner et al. (2008) southernmost. The Hovmoller diagram at 21.5 and 24° N from both AVISO and HYCOM points out the strong reversal of positive and negative anomalies along the eastern side of the basin followed by wave emission. The onset of positive anomalies happens in early November with the wake of the winter monsoon and is likely linked with a moving front of Arabian Sea High Salinity Water, Bay of Bengal water and possibly the effect of river plumes. Those two light density waters occupy the surface creating a time varying shear, a pressure anomaly which can emit Rossby waves.

These waves along 21.5° N are stopped near between 62 and 64° E by a topographic ridge. On 24° N as well, anomalies intensify after 64° E. To study the influence of the topography we used a numerical model of a two dimensional flow in a biperiodic domain and we initialized Rossby waves with a wave length of 180 km, propagating over a sea mount with a 30 km radius. Figure 9 shows the relative vorticity of the flow about every week. The Rossby waves deform over the sea mount and create a dipole propagating westward, the analytical solution for the flow over the sea mount is calculated and described in Appendix B. These results correspond to the propagation observed on the Hovmoller diagram, with anomalies of about 5 cm on the eastern side of the topographic ridge, followed by westward propagating anomalies of more than 15 cm on the western side.

Penetration of Kelvin waves along the coast of India from the Bay of Bengal is known to emit Rossby Waves in the southern part of the basin. A comparison between Rao et al. (2002) years of strong emitting Rossby waves and northern Hovmuller diagram from AVISO emphasizes the fact that Kelvin waves end before 18° N.

4.2 Eddy structure

The eddies are stronger along the northern and western coasts of the Arabian Sea and have radii of about 100 km (see Fig. 10). These eddies are intensified in the upper water column, with velocities up to 0.7 m s^{-1} from the surface down to 150 m depth (see Fig. 11). The velocity section clearly shows the strong vertical influence of those

eddies, down to 2000 m depth. This vertical influence was also seen in L'Hégaret et al. (2013) with the strong correlation between the float drifts at 700 m and the surface geostrophic velocities.

Under the anticyclone and the cyclone, the vertical spacing between isopycnals shrinks and widens successively with a stronger deviation on the first 300 m. These isopycnal deviations have an influence on the water masses. The surface water, Arabian Sea High Salinity Water is sampled on the first 150 m; below, the Indian Central Water is colder and fresher with salinity under 36 psu, and between 200 and 300 m the Persian Gulf Water is observed. The core of Indian Central Water is thinner on HYCOM than on the in situ observations because of the depth of the PGW, which is found deeper (near 250 m). The eddies can deepen or elevate the depth of the PGW; (on Fig. 11) the core is observed at 240 m under the anticyclone and 190 m under the cyclone. Between the eddies layers of ASHSW and ICW wrap around the cyclone, injecting different water masses inside the eddy. The stratification is maximum at the depth of the PGW core and near the injection around the eddies.

4.3 Eddy life cycle

As seen earlier, the eddies form along the different coasts and propagate westward. We review here the different interactions that can occur during the life cycle of those eddies.

4.3.1 Eddy–eddy interactions

As they arrive along the western coast, the eddies tend to propagate southwestward with the exception of a location between Ra's Madrasah (19° N) and North of the mouth of the Sea of Oman (25° N) where the eddies remain fairly stationary between 3 and 4 months. A train of eddies propagates from the eastern basin, anticyclones with a southwestward motion and cyclones with a northwestward one (see Morrow et al., 2004). Those numerous eddies interact in different ways.

Mesoscale variability in the Arabian Sea

P. L'Hégaret et al.

Title Page

Abstract

Introduction

Conclusions

References

Tables

Figures



Back

Close

Full Screen / Esc

Printer-friendly Version

Interactive Discussion



Mesoscale variability in the Arabian Sea

P. L'Hégaret et al.

Title Page

Abstract

Introduction

Conclusions

References

Tables

Figures

◀

▶

◀

▶

Back

Close

Full Screen / Esc

Printer-friendly Version

Interactive Discussion



Two eddies with the same polarity getting close enough, with a distance between their center smaller than 4 times their radius can merge. Figure 12, shows the MADT anomaly during the merging of the two anticyclones, separated in time by a month and a half. The centers of the eddies turn anticyclonically around each other to form the remaining structure. When this merger happens in the center of the basin the final eddy is larger than each of the earlier ones. Nevertheless when it happens near the coast, the final eddy has a size similar to that of the initial eddies (a radius of about 100 km). This is due to the filamentation accompanying merger, and which is amplified in the coastal velocity shear.

The second line of Fig. 13 shows the local turbulent kinetic energy. Before the merging, the maximum of energy is located at the front between the two eddies. After the merging, the maximum of turbulent kinetic energy remains around the anticyclone with the same order of magnitude (about $6 \text{ m}^2 \text{ s}^{-2}$).

The Okubo–Weiss parameter (Fig. 13 third line) is defined as $OW = \sigma_{\text{strain}}^2 + \sigma_{\text{shear}}^2 - \omega^2$ with $\sigma_{\text{strain}} = \frac{\partial V}{\partial x} + \frac{\partial U}{\partial y}$ the strain, $\sigma_{\text{shear}} = \frac{\partial U}{\partial x} - \frac{\partial V}{\partial y}$ the shear and $\omega = \frac{\partial V}{\partial x} - \frac{\partial U}{\partial y}$ the relative vorticity. When OW is positive the deformation dominates and when it is negative the rotation dominates. Merger occurs in a region of strong deformation and rotation; between the two eddies before the merging and at the exterior of the anticyclone afterwards the OW field is mainly positive, revealing a strong deformation around the structures. Inside the anticyclone and principally before the merging, regions of about 50 km in diameter present negative OW thus indicating a recirculation inside the structure.

The anomaly of Ertel Potential Vorticity (PVE hereafter) is computed from

$$\text{PVE} = \frac{1}{\rho_0} \cdot \left(- \left[f + \frac{\partial V}{\partial x} - \frac{\partial U}{\partial y} \right] \cdot \frac{\partial \rho}{\partial z} + \frac{\partial V}{\partial z} \cdot \frac{\partial \rho}{\partial x} + \frac{\partial U}{\partial z} \cdot \frac{\partial \rho}{\partial y} \right)$$

from which we subtract a PVE value calculated out of the eddies (here at the South-East of the region of interest). This anomaly is plotted on the fourth line of Fig. 13. Before merger, the PVE anomaly in the interior of the anticyclone is negative, but the

Mesoscale variability in the Arabian Sea

P. L'Hégaret et al.

Title Page

Abstract

Introduction

Conclusions

References

Tables

Figures

◀

▶

◀

▶

Back

Close

Full Screen / Esc

Printer-friendly Version

Interactive Discussion



region with high positive values of OW presents positive PVE anomaly. This structure is described in Morel and McWilliams (1997) as a R-vortex, where the rotation in the potential vorticity dominates over the stretching. After the merging, the PVE field is less turbulent, keep a R-vortex structure with positive anomalies with low intensity except close to the coast, along the negative altimetric “belt”.

When two eddies with opposite vorticity interact, they create a strong current between them. Also when they have a strong difference of intensity, the strongest one advects the other around. As an example, the anticyclone recorded on altimetry (Fig. 13, top, right) at 24.5° N; 62.7° E propagates from the East for 3 months at an average velocity of 2.5 cm s⁻¹. Then it interacts with the cyclone near 23° N; 60.7° E which presents an angular velocity of 50 cm s⁻¹ and has been stationary for several months. This cyclone accelerates the propagation of the anticyclone at a velocity of 12.4 cm s⁻¹ for a month, advecting it inside the Sea of Oman.

4.3.2 Eddy–surface fluxes (net heat and wind) interaction

Over the seasons the surfaces fluxes have a strong influence on the basin circulation. The wind has an influence on the surface level anomaly through the wind work $P = \boldsymbol{\tau} \cdot \mathbf{U}_g$ with U_g the geostrophic speed at the surface. Roquet et al. (2011) decompose the wind work into a downward flux of pressure work term and a lateral divergence term. Only the first term P_{down} can locally modify or create sea surface anomalies. Following Vic et al. (2014) we integrated this quantity over a mesoscale eddy, $P_{\text{down}} = -\rho_0 g \left\langle \eta \nabla \wedge \left(\frac{\boldsymbol{\tau}}{\rho_0 f} \right) \right\rangle$ with $\langle \cdot \rangle = \frac{1}{S} \iint_S \cdot dS$ and S the surface of the eddy where the MADT anomaly η is larger than 5 cm (this value was chosen to have a closed, delimited contour around the structure).

Haney et al. (2001) studied the transfer of kinetic energy from the vertical shear flow to the vertical mean flow in California Current eddies, that is the baroclinic to barotropic energy conversion (see also Vic et al., 2014). The velocity is decomposed as $U = \bar{u} + u'$ with \bar{u} the barotropic flow and u' the baroclinic. The $(\bar{\cdot})$ is the vertical mean

Mesoscale variability in the Arabian Sea

P. L'Hégaret et al.

Title Page

Abstract

Introduction

Conclusions

References

Tables

Figures



Back

Close

Full Screen / Esc

Printer-friendly Version

Interactive Discussion



defined as $(\bar{\cdot}) = \frac{1}{H} \int_{-H}^0 \cdot dz$ where H is the depth to the surface where more than 50% of the kinetic energy is contained. The kinetic energy conversion $\{K'\bar{K}\}$ is the sum of two terms: $\{K'\bar{K}\}_{\xi} = \rho_0 H \left\langle \nabla \wedge \mathbf{u}' (\bar{u}v' - \bar{v}u') \right\rangle$ and $\{K'\bar{K}\}_{\nabla} = -\rho_0 H \left\langle \nabla \cdot \mathbf{u}' (\bar{u}u' + \bar{v}v') \right\rangle$. The first term is related to the relative vorticity of the shear flow and the second to its divergence. In quasi geostrophic flows the divergence term $\{K'\bar{K}\}_{\nabla}$ is expected to be smaller than $\{K'\bar{K}\}_{\xi}$ (see Haney et al., 2001). We followed 4 anticyclonic mesoscale eddies that stay in the same position during the spring intermonsoon. They had $\{K'\bar{K}\}_{\xi}$ that varied between about 2×10^{-4} and $4 \times 10^{-3} \text{ W m}^{-2}$ and $\{K'\bar{K}\}_{\nabla}$ is about 7×10^{-5} to $5 \times 10^{-4} \text{ W m}^{-2}$, keeping a ratio of 2 to 8 between the term of transfer to the barotropic energy due to vorticity and the one due to divergence. We will focus here on following an eddy where the energy transfer is positive.

Figure 14 represents the time series of this diagnostics. On this figure, we can observe two phases of deepening, between day 12 and 32 and between day 43 and 53 of about 100 m. Those two periods also present an increasing of the wind work P_{down} . The turbulent windstress induced a deepening of the eddy. Those phases of deepening are also associated with oscillations of the term of barotropic energy transfer $\{K'\bar{K}\}_{\xi}$. From day 32 to 42 the eddy became shallower with a strong decrease of $\{K'\bar{K}\}_{\xi}$.

The eddy was followed during the spring intermonsoon season thus having an increase of the net heat flux. The time series of the temperature (see 14, third line) show strong correlations between the variation induced by the net heat flux and the variation of temperature measured at the surface. But few correlations were observed between the depth of the eddies and the temperature variation.

Figure 15 presents the slopes of the wind work, the transfer term from baroclinic to barotropic kinetic energy and the net heat flux compared to the slope of the eddies depth followed during the spring intermonsoons. We observe that for negative depth slope (deepening of the eddies) the sum of wind work and $\{K'\bar{K}\}_{\xi}$ is positive in tendency, mainly due to P_{Down} . Other factors, such as an eddy merger can occur

but the effect of the wind on the vertical signature of the eddy is not negligible on the barotropization of the eddies. As well, during a deepening the slope of the net heat flux is positive, thus indicating a gain of temperature.

When the depth of the eddy remains constant ($\frac{\partial h}{\partial t} \approx 0$), the term of barotropic energy transfer remains low.

For positive values of the depth slope (shallowing of the eddies), both positive and negative values of the sum of barotropization terms are found. The strongest values are positive and principally due to the $\{K' \bar{K}\}_\xi$ term. The net heat flux is negative in tendency for shallowing of the eddies, thus indicating a loss of temperature.

4.3.3 Eddy–Rossby wave interaction

In the HYCOM model, a specific flow configuration is observed near 24° N; 60° E. A pair of mesoscale, surface-intensified, anticyclonic and cyclonic eddies, interact with a Rossby wave, indicated by the peaks of alternating polarity in the SSH field (at approximately 24° N 62–65° E, see Fig. 8). The observed Rossby wave have a limited meridional wavelength and only interacts with the northern, anticyclonic, eddy.

Our purpose is to understand if the wave train, propagating westward and eventually encountering the eddies, can reinforce them or not. Furthermore, the surface dynamics resulting from the interaction will be observed and discussed.

We used here a primitive equation model, ROMS (see Shchepetkin and McWilliams, 2005; Penven et al., 2010, idealized configuration) in which both the anticyclone and the Rossby wave train are initialized by means of analytical functions. Parametrization of this study is described in Appendix C.

The upper left panels in Figs. 16 and 17 are representative of the initial state of the simulation. Two mesoscale eddies are located in the western part of the basin, while the Rossby wave train is given by the peaks of alternating polarity occupying the eastern region. In this configuration, the vortex pair orientation is chosen to obtain a collision with the Rossby wave train. In the realistic case, as shown by the HYCOM model, the dipole orientation, coastal effects and surrounding currents maintain the vortices at

their original position and due to its meridional wavelength the Rossby wave train only interacts with the northern eddy.

The analysis of ERTTEL PV anomaly fields does not suggest any reinforcing of the anticyclonic eddy. Figure 18 shows the modulus of anticyclonic PV anomaly as a function of time. Apart from a slight increase registered between 5 and 10 days, the trend is decaying over the time scale of one month. Therefore, the earlier interpretation of anticyclone reinforcement by a Rossby wave (see L'Hégaret et al., 2013) does not seem supported by the present simulations.

Furthermore, since the early stages of the evolution, the dipole starts interacting with the Rossby wave with consequent generation of a circular envelope of potential vorticity around it. The sign of the envelope changes in the northern and southern edge of the dipole, with consequent squeezing of the dipole and enhancement of the translational velocity across the basin (as also observed in Couder and Basdevant, 1986).

Filamentation and generation of eddies is also observed and results from the straining of the PV field associated to the wave train. In particular, looking at the lower right panel of Figs. 16 and 17, closed contours in SSH and ERTTEL PV surface fields are observed around the points $X_1 = (x = 400 \text{ km}, y = 200 \text{ km})$ and $X_2 = (x = 400 \text{ km}, y = 600 \text{ km})$ and are indicators of eddy-like features with diameters around 50 km.

5 Interaction of the mesoscale eddies with Persian Gulf Water

In this section we focus on the impact of the mesoscale eddies on the Persian Gulf Water outflow, principally in the Sea of Oman. Through the Strait of Hormuz, the PGW outflow exits the Persian Gulf as a dense bottom water mass, with salinity larger than 40 psu in the Strait and flanks the western coast.

Mesoscale variability in the Arabian Sea

P. L'Hégaret et al.

Title Page

Abstract

Introduction

Conclusions

References

Tables

Figures



Back

Close

Full Screen / Esc

Printer-friendly Version

Interactive Discussion



5.1 Trajectory and ejection

Figure 19 represents the variations of the PGW depth (left) and salinity (right). The first EOF, with a representativity of 41 %, shows a variation of 60 m of the depth of the PGW North of Ra's Al Hadd, with a deepening in spring and a shallowing in late summer to fall. This variation is strongly correlated with the second and third EOFs of the altimetry (see Fig. 4) which showed the presence of an anticyclone in spring and a cyclone in winter; the anticyclone that deepens the isopycnals and the cyclone shallowing them. On the second and third EOFs of the PGW depth (Fig. 19, left), with representativity of 6.6 and 4.9 %, variability is found between Ra's Al Hamra and Ra's Al Hadd, with a shallowing in winter in the center of the Sea of Oman and a deepening from late spring to summer. Those tendencies can also be linked with the first EOF from Fig. 4 with the positive belt in winter and the stationnary cyclone at the mouth of the Sea of Oman.

The right hand side of Fig. 19 highlights the salinity variations of the PGW. The three first EOFs, which represent respectively 20, 7.9 and 7.2 % of the PGW salt variation have in common the strong gradient in the western Sea of Oman (West of 58° E). The PGW outflow, with the strongest salinities, is constrained in the northwestern part of the basin during spring and early summer. On the first EOF, this variation deviates along the northern coast, indicating a recirculation to the North, induced by the anticyclone North of Ra's Al Hadd. Again on this EOF, a strong variation is observed from late summer to the end of the winter around Ra's Al Hadd, thus indicating a presence a PGW during this period. The second and third EOFs show the pathways of the PGW, along the southern coast from Ra's Al Hamra to Ra's Al Hadd, with either an ejection (second EOF, occurs in summer), or a propagation southward along the coast of Oman (third EOF, during winter). In summer, the PGW outflow follows the southern coast from its equilibrium, whereas in winter it is ejected from the northern coast. The pathway of the PGW, revealed here by its salinity is strongly correlated with the EOF of the

Title Page

Abstract

Introduction

Conclusions

References

Tables

Figures



Back

Close

Full Screen / Esc

Printer-friendly Version

Interactive Discussion



altimetry, with the recirculation on the western side of the basin and the ejection site; the PGW pathway is constrained by the mesoscale eddies.

Forced by the surface eddies, the PGW can have different pathways and ejection site from the coast. Figure 20 presents the trajectories of the PGW maximum at 4 different months (for each season). From the Strait of Hormuz to 25° N all pathways are similar, the PGW being constrained by the sill. August and October have the same trajectories, with ejection at Ra's Al Hadd. In January, the pathway is first North, then detaches from the coast after 56° E recirculates northward, and then is advected South. In early winter, when the PGW detaches from the coast, it can form anticyclonic lee eddy (see Verron et al., 1991). In May, the PGW detaches from the coast near Ra's Al Hamra (see L'Hégaret et al., 2013).

5.2 Characteristics

Figure 21 presents the geometrical structure and dilution of the PGW outflow along the four different months characteristic of each seasons. The thickness and width are estimated using the method of Pous et al. (2004b), with the limit being the isohaline ($\frac{S_{PGW} + S_{env}}{2}$) with S_{PGW} the salinity of the PGW core and S_{env} the salinity of the surrounding water mass. For the first 100 km of the pathway the depth of the PGW remains constant before sinking. This deepening is accompanied by strong increases in thickness and width.

In winter, the PGW dives to equilibrate at 200 m depth; this deepening is followed by an increase of thickness, from 25 m to almost 200 m before remaining around 120 m depth. Its width remains nearly constant at about 50 km. This strong change in PGW characteristics is also accompanied by a strong dilution. Before sinking, the PGW salinity is higher than 40 psu, then it decreases down to 38 psu when the water mass equilibrates. In temperature, after a first increase above 25 °C due to a mixing with the surrounding waters, it decreases below 23 °C at the position of equilibrium. Those characteristics reveal that the outflow remains as a core along the northern part of the basin.

Mesoscale variability in the Arabian Sea

P. L'Hégaret et al.

Title Page

Abstract

Introduction

Conclusions

References

Tables

Figures



Back

Close

Full Screen / Esc

Printer-friendly Version

Interactive Discussion



They are comparable with the results of measurements from the GOGP experiment described in Pous et al. (2004b).

In spring, the outflow salinity and temperature are lower with values of 40 psu and 22 °C. After the deepening, mixing results in a small increase of temperature first. The outflow sinks below its winter depth of equilibrium, about 250 m. For about 150 km after the deepening, the thickness of the water mass increases to 200 m and then decreases to 100 m. The PGW core width is above 150 km, indicating a recirculation in the western basin, then it decreases strongly to 50 km and re-increases just after. This decrease corresponds to the closest point of the outflow trajectory towards the coast. After its recirculation eastward, the outflow is ejected from Ra's Al Hamra and spreads in the basin.

The third line of Fig. 21 shows the summer characteristics. Mixing starts at 100 km from the initial point at the Straits, from almost 40 psu and 24 °C, directly followed with a small increase of the temperature to 26 °C. These thermohaline characteristics decrease slowly after 300 km to 37 psu and below 22 °C. From 100 to 300 km of the initial point, the depth of the PGW decreases slowly to 200 m. Its thickness increases from 20 to 140 m and then decreases down to 80 m; its width enlarges up to 100 km. After 300 km path the thickness and width stay almost constant around 120 m and 60 km; the outflow shallows around 180 m. Those characteristics indicates that after the Strait of Hormuz, the outflow recirculates in the south-western part of the basin before flowing out of the basin off Ra's Al Hadd under the influence of the cyclone present in summer, thus explaining the shallowing, widening and slowing down of the dilution.

Finally in fall, those characteristics are very similar to those of summer, with fewer recirculations in the western part and an earlier influence of the cyclone North of Ra's Al Hadd, with a narrowing of the outflow downstream Ra's Al Hamra.

To summarize, the thermohaline characteristics of the PGW outflow in the western part of the basin show variation due to their mixing right after the sill. Often temperature first increases, then all characteristics decrease, the core deepens, widens before other variations due to surface eddies take place. Nevertheless, the time of residence

Mesoscale variability in the Arabian Sea

P. L'Hégaret et al.

Title Page

Abstract

Introduction

Conclusions

References

Tables

Figures



Back

Close

Full Screen / Esc

Printer-friendly Version

Interactive Discussion



**Mesoscale variability
in the Arabian Sea**

P. L'Hégaret et al.

Title Page

Abstract

Introduction

Conclusions

References

Tables

Figures



Back

Close

Full Screen / Esc

Printer-friendly Version

Interactive Discussion



and pathways of PGW in the Sea of Oman are strongly influenced by the seasons. Three different locations of PGW ejection have been observed (see Fig. 22): along the northern (Iranian) coast in winter without recirculation westwards, whereas in spring and summer this ejection advects PGW south-westward. In spring an ejection is observed off Ra's Al Hamra, with a marked anticyclonic circulation and traces of PGW along both the northern and southern coasts. In summer and fall, this ejection occurs at Ra's Al Hadd, with a stronger front in summer and a cyclonic advection.

Those ejections consequently tear the PGW outflow and fragment the water mass to form filaments and lenses. PGW can also be found inshore via the formation of a lee eddy near Ra's Al Hamra (first panel of Fig. 22) or it can be advected inside the core of an eddy (as in summer) with stronger dilution of the water mass. The lens measured in Senju et al. (1998) is similar to the lee eddy in position, between Ra's Al Hamra and Ra's Al Hadd, size, about 100 km in diameter, and salinity, diluted PGW at 36.8 psu.

6 Conclusions

In this paper we address the problem of seasonal variability of the mesoscale eddies in the Arabian Sea and Sea of Oman. We compared the HYCOM model outputs and measurements from satellites, floats and climatology. Notable similarities were found on the water masses thermohaline characteristics and altimetric signature. The surface circulation is highly seasonal under the influence of the wind stress, creating strips of SSH anomaly along the coasts, positive in winter, negative in summer. This strip deforms to form mesoscale eddies propagating westward with a strong barotropic component. It also creates Rossby waves along the coast of India that form eddies after crossing the rift in the Arabian Sea.

The mesoscale eddies interact in different ways across the basin. Two close eddies with the same polarity can merge to form a larger structure; nevertheless near the coast the final eddy often has a size similar to the earlier ones. Two eddies with opposite polarity advect each other as dipoles. The wind influences the deepening and

**Mesoscale variability
in the Arabian Sea**

P. L'Hégaret et al.

Title Page

Abstract

Introduction

Conclusions

References

Tables

Figures



Back

Close

Full Screen / Esc

Printer-friendly Version

Interactive Discussion



barotropization of the eddies. The net heat fluxes also showed a gain or loss of heat with the deepening or shallowing of the eddies depth. A simulation of the interaction between Rossby waves and mesoscale eddies showed a limited impact of the waves on the eddies, but the creation of filaments and smaller eddy-like structures. Further modeling will provide a better understanding of these mechanisms.

The Persian Gulf outflow is impacted by the mesoscale eddies, influencing on its pathway along the Sea of Oman and its ejection sites from the coast, from the Ra's Al Hadd cape in summer, from Ra's Al Hamra in spring and fall and along the northern coast in winter. The thermohaline characteristics are also changed by recirculation in the western part of the basin, by the creation of coastal eddies or by the breaking of the core, these phenomena leading to thermohaline mixing. The injection of PGW inside eddies allows this water mass to keep a stronger thermohaline signature across the Arabian Sea, filaments being more subject to erosion.

Thus this study provides a description of the path of PGW outflow from its exit from the Strait of Hormuz to its dispersion in the Arabian Sea. Several types of mesoscale eddies containing PGW (lee eddies, isolate eddies, dipoles) were found, as well as many submesoscale structures (small eddies and filaments). Further investigation of these submesoscale structures using in-situ data of the Phys-Indien experiments, and the analysis of fine scale intrusions at thermohaline fronts, will be the subject of a forthcoming paper.

Appendix A: Surfaces fluxes and thermodynamics**A1 Winds**

The winter monsoon lasts from November to early February; then, winds reverse and blow from the North-East (up to 6 ms^{-1}) but they keep a stable orientation. In the northern part of the basin, the winds are very weak. The surface circulation is cyclonic near the center of the Arabian Sea, characterised by a negative anomaly of altimetry.

**Mesoscale variability
in the Arabian Sea**

P. L'Hégaret et al.

Title Page

Abstract

Introduction

Conclusions

References

Tables

Figures

I◀

▶I

◀

▶

Back

Close

Full Screen / Esc

Printer-friendly Version

Interactive Discussion



In spring, the inter monsoon transition is slower than in fall. First, the orientation and intensity of the winter monsoon winds decrease and vanish from West to East, starting in February until end of March (see Fig. 23). During this period, winds are almost zero near the southern Omani coast and up to 64° E. Then, from March to May, the onset of the summer monsoon progresses from the North-West to the South-East of the Arabian Sea.

The summer monsoon lasts from May to September in the Arabian Sea, with winds blowing from the South-West, intensifying in July and August with stronger velocities than in winter (reaching velocities up to 10 ms^{-1} , see Fig. 23, left). Therefore, opposite to the winter monsoon, the altimetric anomaly is positive in the center of the basin, and negative along the coasts thus creating an anticyclonic circulation. Upwellings are found along the coasts of Somalia, Yemen and Oman leading to colder and fresher water (see Fig. 24).

The fall inter monsoon is relatively short and lasts mostly from the end of September to early November (see Fig. 23). During this period, the winds have little dominant orientation and almost vanish in the center of the Arabian Sea.

A2 Fluxes

The evaporation is strongest during the monsoon seasons, with the strong and regular winds blowing all over the Arabian Sea (see Fig. 25, left). In summer, the southwestern winds bring strong precipitation towards the western Ghats, the chain of mountains South-West of India, for over 2 equivalent meters. Furthermore, those fresh waters join the river runoff and participate to provide low saline waters along the western coast of India from the end of summer to early winter. With this exception aside, evaporation dominates precipitation year round all over the northwestern Indian Ocean. In the Arabian Sea, the maximum of evaporation occurs in winter on the northeastern part and it stays strong in the Sea of Oman with a local minimum around the eastern part of Oman from spring to early summer.

Mesoscale variability in the Arabian Sea

P. L'Hégaret et al.

Title Page

Abstract

Introduction

Conclusions

References

Tables

Figures



Back

Close

Full Screen / Esc

Printer-friendly Version

Interactive Discussion



With those monthly averaged fluxes of evaporation over precipitation we can estimate the variation of the surface salinity over a month via: $\frac{dS}{dt} = S_0 \frac{E-P}{H}$ with S_0 an averaged surface salinity extracted from the climatology, E and P the evaporation and precipitation in equivalent meter and H the depth of the mixed layer. This depth is the density derived mixed layer. This is defined as the depth where the density has increased to a value of density with a 0.2°C variation. The variations of salinity over a month are low, up to 1.5×10^{-3} psu per month. Those peaks correspond to a gain in salinity and are mainly along the coast of India (South in winter and spring, and North in summer and fall) and in the Sea of Oman. Variations of 1×10^{-3} psu per month can also be found locally in mesoscale structure across the basin. Those values are positive all year long with the exception of summer, where the monsoon along India brings fresher water and a decrease of salinity up to -4×10^{-3} psu per month.

The net heat flux follows the budget of evaporation and precipitation (see Fig. 25, right). In winter there is a maximum of heat loss over the northwestern Indian ocean with a mean of -250 W m^{-2} , leading to the formation of the Arabian Sea High Salinity Water near the surface, as on Fig. 24 where strong salinities are spreading South. During the inter monsoon seasons the Arabian Sea lose heat, particularly over 24°N , between -100 and -150 W m^{-2} . In summer, this flux attenuates and the Arabian Sea loses less heat, with local minima of loss through the mouth of the Sea of Oman and along the southern coast of Pakistan, having values up to -50 W m^{-2} and even heat gain near the eastern coast of Oman, at the location of the upwellings. All year long the northern and western parts of the Sea of Oman show local maxima of heat loss. Oppositely the eastern coast of Oman, South of Ra's Al Hadd show local minima of heat loss, particularly in the monsoon seasons.

As for the variation of salinity, we can estimate the variation of the surface temperature over a month via thermodynamics: $\frac{dT}{dt} = \frac{Q_{\text{net}}}{\rho_0 C_w H}$ with Q_{net} the net heat flux, ρ_0 the water density, C_w the heat capacity for water (here $C_w = 4.18 \times 10^{-3} \text{ J kg}^{-1} \text{ K}^{-1}$) and H the density defined mixed layer. Similarly to the surface salinity variation, the Arabian Sea shows a decrease in temperature along the coast of India, in the Sea of Oman

and inside mesoscale structure across the basin, with values up to -3°C per month. The ocean only gains heat in summer in the upwelling region but with values smaller than 1°C per month.

Appendix B: Interaction of a long Rossby wave with a circular seamount

5 In this section, we provide a simple analytical calculation for the interaction of a long, zonal Rossby wave, with a localized, circular (parabolic shaped) seamount. We use the 2-D or barotropic vorticity equation on the β plane with bottom topography

$$\partial_t(\nabla^2\psi) + J(\psi, \nabla^2\psi) + J(\psi, f_0 h_b/H) + \beta \partial_x \psi = 0$$

Our basic flow is a zonal Rossby wave with wavenumber k

10
$$\psi_0(x, t) = A_0 \exp(ik[x - ct]) = A_0 \exp(ik[r \cos(\theta) - ct])$$

which is a solution of the nonlinear vorticity equation over flat bottom with $c = \frac{-\beta}{k^2}$. We also recall that

$$\nabla^2\psi_0 = -k^2\psi_0$$

Furthermore, we assume that the seamount height is small $f_0 h_b/H = \epsilon A_b(r)$ and that it has a radius $r_0 \ll 2\pi/k$.

15 Since the topographic term is small in the vorticity equation, we can look for a response of the flow in terms of a perturbation expansion

$$\psi(x, y, t) = \psi_0(x, t) + \epsilon \psi_1(x, y, t)$$

Thus we have, at order ϵ

20
$$\partial_t(\nabla^2\psi_1) + J(\psi_0, \nabla^2\psi_1) + J(\psi_1, \nabla^2\psi_0) + \beta \partial_x \psi_1 + J(\psi_0, A_b) = 0$$

Title Page

Abstract

Introduction

Conclusions

References

Tables

Figures

◀

▶

◀

▶

Back

Close

Full Screen / Esc

Printer-friendly Version

Interactive Discussion



To simplify this equation further, we assume that $A_b = A_b^0(1 - (r/r_0)^2)$, so that the last term is simply

$$(2A_b^0/r_0^2)\partial_\theta\psi_0 = -2ikr\sin(\theta)(A_0A_b^0/r_0^2)\exp(ik[x - ct]).$$

or, more simply, a term in $y\exp(ik[x - ct])$ that is going to force the flow response in ψ_1 . Thus we assume that

$$\psi_1 = \phi_1 y t \exp(ik[x - ct])$$

Then

$$\nabla^2\psi_1 = -k^2\phi_1 y t \exp(ik[x - ct]) = -k^2\psi_1$$

Therefore the vorticity anomaly over the sea mount is

$$J(\psi_0, \nabla^2\psi_1) + J(\psi_1, \nabla^2\psi_0) = 0$$

Now

$$\partial_t(\nabla^2\psi_1) = (1 - ikct)(-k^2)\phi_1 y \exp(ik[x - ct])$$

and

$$\beta\partial_x\psi_1 = ik\beta\phi_1 y t \exp(ik[x - ct])$$

which cancels out the second term of the time derivative. Therefore

$$-k^2\phi_1 y \exp(ik[x - ct]) - 2iky(A_0A_b^0/r_0^2)\exp(ik[x - ct]) = 0$$

or finally

$$\phi_1 = -2iA_0A_b^0/(kr_0^2)$$

**Mesoscale variability
in the Arabian Sea**

P. L'Hégaret et al.

Title Page	
Abstract	Introduction
Conclusions	References
Tables	Figures
◀	▶
◀	▶
Back	Close
Full Screen / Esc	
Printer-friendly Version	
Interactive Discussion	



The velocity associated with the zonal Rossby wave is meridional $v_0 = \partial_x \psi_0 = ikA_0 \exp(ik[x - ct])$. Therefore

$$\nabla^2 \psi_1 = 2A_b^0 y t v_0 / r_0^2$$

From this, one can see immediately that negative vorticity will be created by a northward motion of the particles ($v_0 > 0$) on the southern side of the seamount ($y < 0$, where the fluid columns will experience squeezing) and conversely on the northern side of the seamount.

If the wavelength of the Rossby wave is long compared with the radius of the seamount, enough perturbation vorticity will build up on these two sides of the seamount and a dipole will be formed which can then detach.

Appendix C: Parametrization and initialization of the ROMS model

The vortex-Rossby wave interaction study has been carried out numerically with the primitive equation model ROMS. In particular, simulations were run in a flat-bottomed semi-closed basin of size (800 km) in the horizontal and 3000 m in the vertical. The chosen stratification for the basin is analytical and it is characterized by a Rossby Radius deformation of about 40 km, typical of our region of interest, (Chelton et al., 1998).

The vertical discretization is given by 80 non-uniformly spaced levels, since a finer vertical resolution has been used for levels closer to the sea surface, where the interaction between the vortex and the Rossby wave takes place. The horizontal resolution is 5 km, which we consider to be appropriate for investigation of a mesoscale process. Minimization of adjustment effects in the first time steps of the simulation requires use of cyclogeostrophic balance for the anticyclone (whose estimated Rossby number is $Ro \simeq 0.6$). The eddy is introduced as an analytical three-dimensional velocity field, expressed by Eq. (C1).

$$v_\theta = \frac{-v_0 r}{R} e^{-\frac{r^2}{R^2}} e^{-\frac{(z-z_0)^2}{H^2}} \quad (C1)$$

Mesoscale variability in the Arabian Sea

P. L'Hégaret et al.

Title Page

Abstract

Introduction

Conclusions

References

Tables

Figures



Back

Close

Full Screen / Esc

Printer-friendly Version

Interactive Discussion



The Rossby wave has been introduced as a surface intensified perturbation in the pressure field. Its analytical expression is given by Eq. (C2)

$$p'(x, y, z) = \alpha f(x)g(y)h(z) \quad (\text{C2})$$

with

$$\begin{cases} \alpha \approx \rho g \\ f(x) = 1 + \tanh\left(\frac{x-x_{R0}}{\lambda_{R0}}\right) \cos(k_{R0}x) \\ g(y) = \sin\left(\frac{\pi y}{L}\right) \\ h(z) = e^{-\left(\frac{z}{H_{R0}}\right)^2} \end{cases} \quad (\text{C3})$$

The parameters for the initialization of the anticyclonic eddy and the Rossby wave have been chosen following the HYCOM model outputs, and are summarized in Table 1.

The simulation is run on a planetary β plane. The initial state, as well the evolution in time of the flow configuration, are shown in Figs. 16 and 17.

References

- Bower, A. S., Hunt, H. D., and Price, J. F.: Character and dynamics of the red Sea and the Persian Gulf outflows, *J. Geophys. Res.-Oceans*, 105, 6387–6414, 2000. 495
- Carnes, M. R.: Description and Evaluation of GDEM-V 3.0, Naval Research Laboratory, Oceanography Division, Stennis Space Center, MS 39529-5004, 2009. 497
- Carton, X., L'Hégaret, P., and Baraille, R.: Mesoscale variability of water masses in the Arabian Sea as revealed by ARGO floats, *Ocean Sci.*, 8, 227–248, doi:10.5194/os-8-227-2012, 2012. 495
- Chassignet, E. P., Hurlburt, H. E., Smedstad, O. M., Halliwell, G. R., Hogan, P. J., Wallcraft, A. J., Baraille, R., and Bleck, R.: The HYCOM (HYbrid Coordinate Ocean Model) data assimilative system, *J. Marine Syst.*, 65, 60–83, 2007. 496

- Chelton, D., De Szoeke, R., Schlax, M., El Naggar, K., and Siwertz, N.: Geographical variability of the first baroclinic rossby radius of deformation, *J. Phys. Oceanogr.*, 28, 433–459, 1998. 520
- Couder, Y. and Basdevant, C.: Experimental and numerical study of vortex couples in two-dimensional flows, *J. Fluid Mech.*, 173, 225–251, 1986. 510
- Defant, A.: *Physical Oceanography*, Pergamon Press, Oxford, UK, 2, 1961. 495
- Dong, C., McWilliams, J. C., and Shchepetkin, A. F.: Island wakes in deep water, *J. Phys. Oceanogr.*, 37, 962–981, 2007. 503
- Flierl, G. R., Carton, X. J., and Messenger, C.: Vortex formation by unstable oceanic jets, *European Series in Applied and Industrial Mathematics: Proceedings*, 7, 137–150, 1999. 503
- Haney, R. L., Hale, R. A., and Dietrich, D. E.: Offshore propagation of eddy kinetic energy in the California Current, *J. Geophys. Res.-Oceans*, 106, 11709–11717, 2001. 507, 508
- Heffner, D. M., Subrahmanyam, B., and Shriver, J. F.: Indian Ocean Rossby waves detected in HYCOM sea surface salinity, *Geophys. Res. Lett.*, 35, published online first, doi:10.1029/2007GL032760, 2008. 504
- Johns, W., Yao, F., Olson, D. B., Josey, S. A., Grist, J. P., and Smeed, D. A.: Character and dynamics of the red Sea and the Persian Gulf outflows, *J. Geophys. Res.-Oceans*, 105, 6387–6414, 2000. 495
- Kumar, S. P. and Prasad, T. G.: Formation and spreading of Arabian Sea high-salinity water mass, *J. Geophys. Res.-Oceans*, 104, 1455–1464, 2012. 501
- Kumar, R. R., Kumar, B. P., Satyanarayana, A. N. V., Subrahmanyam, D. B., Rao, A. D., and Dube, S. K.: Parameterization of sea surface drag under varying sea state and its dependence on wave age, *Nat. Hazards*, 49, 187–197, 2009. 498
- L'Hégaret, P., Lacour, L., Carton, X., Rouillet, G., Baraille, R., and Correard, S.: A seasonal dipolar eddy near Ras Al Hamra (Sea of Oman), *Ocean Dynam.*, 63, 633–659, 2013. 496, 503, 505, 510, 512
- Matsuyama, M., Kitade, Y., Senjyu, T., Koike, Y., and Ishimaru, T.: Vertical Structure of a Current and Density Front in the Strait of Hormuz, *C3, Terrapub, Tokyo*, 23–34, 1998. 495
- Morel, Y. and McWilliams, J.: Evolution of isolated interior vortices in the ocean, *J. Phys. Oceanogr.*, 27, 727–748, 1997. 507
- Morrow, R., Birol, F., Griffin, D., and Sudre, J.: Divergent pathways of cyclonic and anti-cyclonic ocean eddies, *Geophys. Res. Lett.*, 31, published online first, doi:10.1029/2004GL020974, 2004. 505

**Mesoscale variability
in the Arabian Sea**

P. L'Hégaret et al.

Title Page

Abstract

Introduction

Conclusions

References

Tables

Figures



Back

Close

Full Screen / Esc

Printer-friendly Version

Interactive Discussion



**Mesoscale variability
in the Arabian Sea**

P. L'Hégaret et al.

Title Page

Abstract

Introduction

Conclusions

References

Tables

Figures



Back

Close

Full Screen / Esc

Printer-friendly Version

Interactive Discussion



- Penven, P., Cambon, G., Tan, T.-A., Marchesiello, P., and Debreu, L.: ROMS AGRIF/ROMSTOOLS User's Guide, Tech. rep., IRD (Institut de Recherche pour le Developpement), Marseille, France, 2010. 509
- 5 Pous, S. P., Carton, X., and Lazure, P.: Hydrology and circulation in the Strait of Hormuz and the Gulf of Oman results from the GOGP99 experiment: 1. Strait of Hormuz, *J. Geophys. Res.-Oceans*, 109, 1978–2012, 2004a. 495
- Pous, S. P., Carton, X., and Lazure, P.: Hydrology and circulation in the Strait of Hormuz and the Gulf of Oman results from the GOGP99 experiment: 2. Gulf of Oman, *J. Geophys. Res.-Oceans*, 109, 1978–2012, 2004b. 495, 512, 513
- 10 Rao, S. A., Behera, S. K., Masumoto, Y., and Yamagata, T.: Interannual subsurface variability in the tropical Indian Ocean with a special emphasis on the Indian Ocean dipole, *Deep-Sea Res. Pt. II*, 49, 1549–1572, 2002. 504
- Roquet, F., Wunsch, C., and Madec, G.: On the patterns of wind power input to the ocean circulation, *J. Phys. Oceanogr.*, 41, 2328–2342, 2011. 507
- 15 Schott, F. A. and McCreary Jr., J. P.: The monsoonal circulation of the Indian Ocean, *Prog. Oceanogr.*, 51, 1–123, 2001. 499
- Schott, F. A., Xie, S. P., and McCreary, J. P.: Indian Ocean circulation and climate variability, *Rev. Geophys.*, 47, published online first, doi:10.1029/2007RG000245, 2009. 495
- Senjyu, T., Ishimaru, T., Matsuyama, M., and Koike, Y.: High salinity lens from the Strait of Hormuz, in: *Offshore Environment of the ROPME Sea Area after the War-Related Oil Spill*, Terrapub, Tokyo, 35–49, 1998. 496, 514
- 20 Shchepetkin, A. F. and McWilliams, J. C.: The Regional Oceanic Modeling System (ROMS): a split-explicit, free-surface, topography-following-coordinate oceanic model, *Ocean Model.*, 9, 347–404, 2005. 509
- Shi, W., Morrison, J. M., Bohm, E., and Manghanani, V.: The Oman upwelling zone during 1993, 1994 and 1995, *Deep-Sea Res. Pt. II*, 47, 1227–1247, 2000. 495
- Smith, K. S.: The geography of linear baroclinic instability in Earth's oceans, *J. Mar. Res.*, 65, 655–683, 2007. 502
- Thoppil, P. G. and Hogan, P. J.: On the mechanisms of episodic salinity outflow events in the Strait of Hormuz, *J. Phys. Oceanogr.*, 39, 1340–1360, 2009. 495
- 30 Vallis, G. K.: *Atmospheric and oceanic fluid dynamics: fundamentals and large-scale circulation*, Cambridge University Press, 2006.

- Verron, J., Davies, P. A., and Dakin, J. M.: Quasigeostrophic flow past a cape in a homogeneous fluid, *Fluid Dynam. Res.*, 7, doi:10.1016/0169-5983(91)90002-Z, 1991. 512
- Vic, C., Rouillet, G., Carton, X., and Capet, X.: Mesoscale dynamics in the Arabian Sea and a focus on the Great Whirl life cycle: a numerical investigation using ROMS, *J. Geophys. Res.-Oceans*, 119, 6422–6439, 2014. 500, 507
- 5 Wang, Z., DiMarco, S. F., Jochens, A. E., and Ingles, S.: High salinity events in the northern Arabian Sea and Sea of Oman, *Deep-Sea Res. Pt. I*, 74, 14–24, 2013. 496
- Yao, F. and Johns, W. E.: A HYCOM modeling study of the Persian Gulf: 1. Model configurations and surface circulation, *J. Geophys. Res.-Oceans*, 115, C11, doi:10.1029/2009JC005781, 2010a. 495
- 10 Yao, F. and Johns, W. E.: A HYCOM modeling study of the Persian Gulf: 2. Formation and export of Persian Gulf Water, *J. Geophys. Res.-Oceans*, 115, C11, doi:10.1029/2009JC005781, 2010b. 495

OSD

12, 493–550, 2015

Mesoscale variability in the Arabian Sea

P. L'Hégaret et al.

Title Page

Abstract

Introduction

Conclusions

References

Tables

Figures

◀

▶

◀

▶

Back

Close

Full Screen / Esc

Printer-friendly Version

Interactive Discussion



Mesoscale variability in the Arabian Sea

P. L'Hégaret et al.

Title Page

Abstract

Introduction

Conclusions

References

Tables

Figures

◀

▶

◀

▶

Back

Close

Full Screen / Esc

Printer-friendly Version

Interactive Discussion



Table 1. Parameters for initialization of the anticyclonic Eddy and the Rossby wave, derived from HYCOM output.

Eddy	Rossby wave
$R = 100 \text{ km}$	$x_{R0} = 350 \text{ km}$
$z_0 = 100 \text{ m}$	$\lambda_{R0} = 200 \text{ km}$
$H = 800 \text{ m}$	$k_{R0} = 2\pi/\lambda_{R0}$
$v_0 = 0.8 \text{ ms}^{-1}$	$H_{R0} = 200 \text{ m}$

**Mesoscale variability
in the Arabian Sea**

P. L'Hégaret et al.

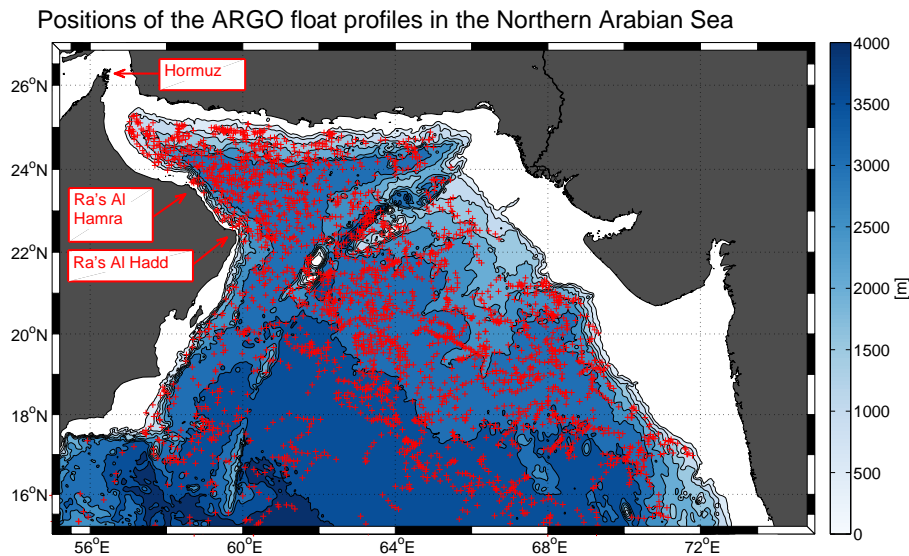


Figure 1. Positions of the ARGO profiles for the 4 months of interest, March, July, October and December, in the northern Arabian Sea, superimposed on bathymetry. The isobaths shown are every 1000 m depth.



Back

Close

Full Screen / Esc

Printer-friendly Version

Interactive Discussion



**Mesoscale variability
in the Arabian Sea**

P. L'Hégaret et al.

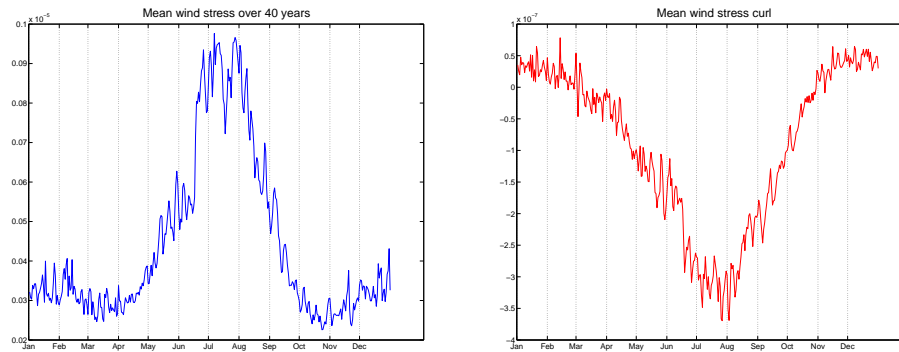


Figure 2. Averaged wind stress (Nm^{-2}) over a 2° square region off Ra's Al Hadd over 40 years (left) and averaged wind stress curl (Nm^{-3} , right) over the same region.

Title Page

Abstract

Introduction

Conclusions

References

Tables

Figures



Back

Close

Full Screen / Esc

Printer-friendly Version

Interactive Discussion



Mesoscale variability in the Arabian Sea

P. L'Hégaret et al.

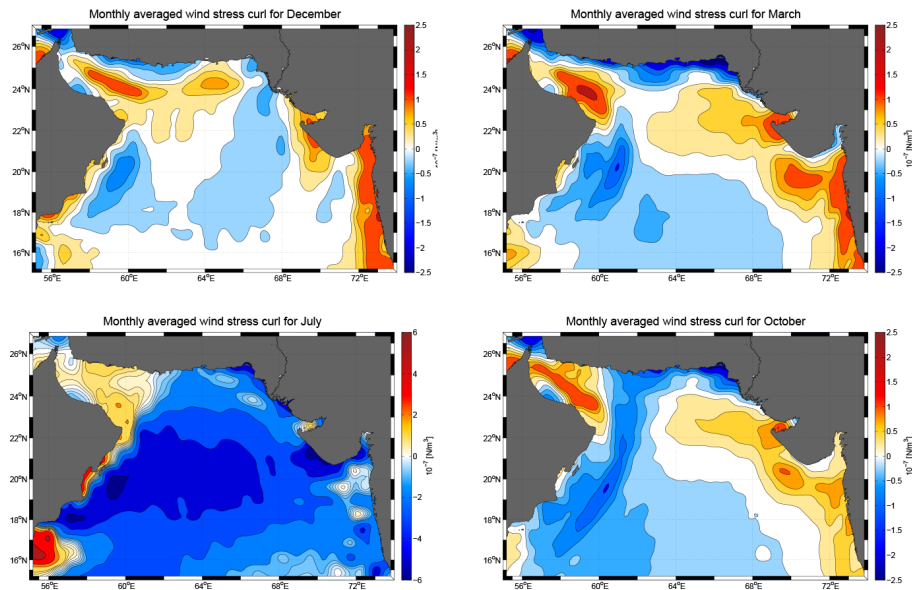


Figure 3. From top to bottom: mean wind stress curl from ECMWF in December, March, July and October.

Title Page

Abstract

Introduction

Conclusions

References

Tables

Figures

◀

▶

◀

▶

Back

Close

Full Screen / Esc

Printer-friendly Version

Interactive Discussion



Mesoscale variability in the Arabian Sea

P. L'Hégaret et al.

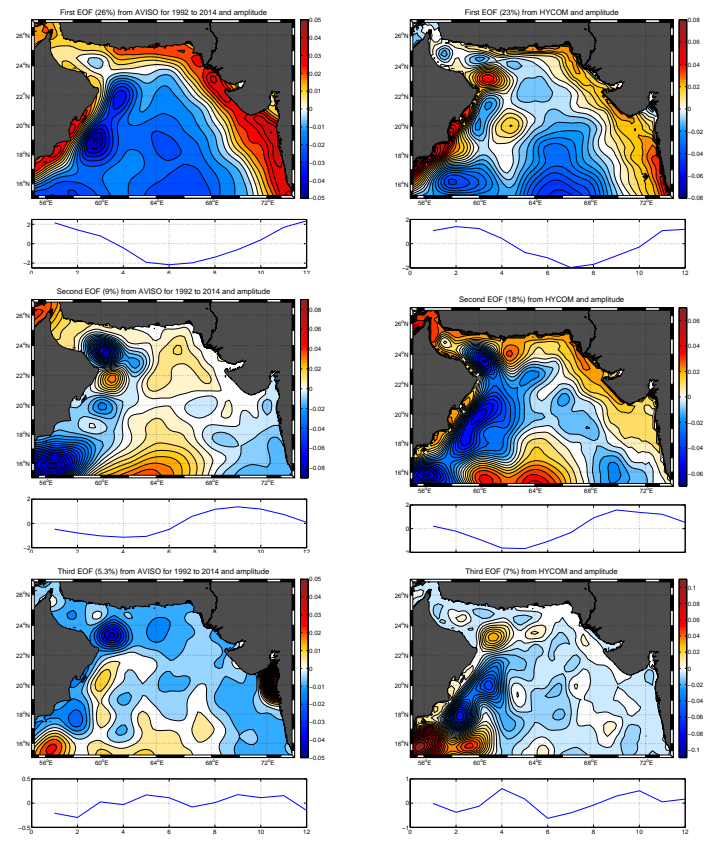


Figure 4. First three EOF's of MADT anomaly, computed with altimetric data using time series of their monthly averaged amplitudes from (right) AVISO from 1992 to 2014 and (left) HYCOM for 6 years.

Title Page

Abstract Introduction

Conclusions References

Tables Figures

◀ ▶

◀ ▶

Back Close

Full Screen / Esc

Printer-friendly Version

Interactive Discussion



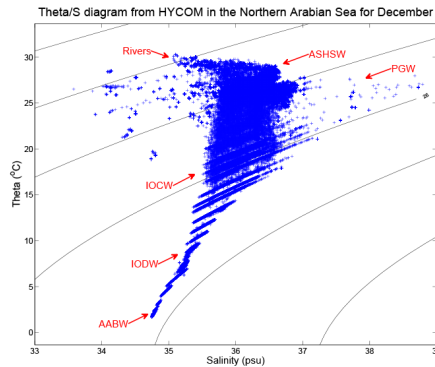
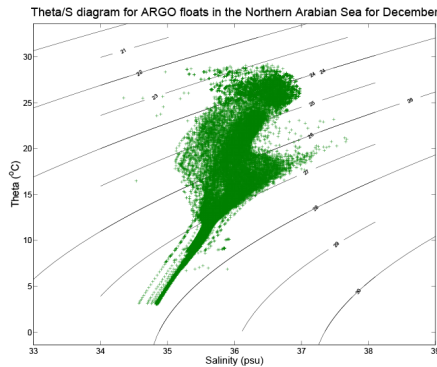
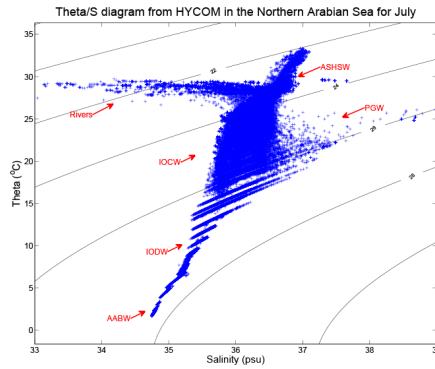
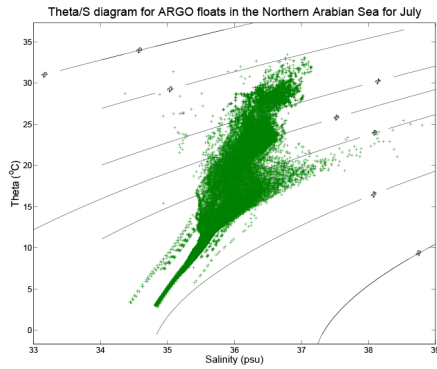


Figure 5. From top to bottom: potential temperature and salinity diagram for the northern Arabian Sea during July and December. On the left side, the diagram corresponds to the ARGO floats measurements; on the right side the values extracted from the HYCOM model. Abbreviations are: PGW: Persian Gulf Water; ASHSW: Arabian Sea High Salinity Water; IOCW: Indian Ocean Central Water; IODW: Indian Ocean Deep Water; AABW: Antarctic Bottom Water.

Mesoscale variability in the Arabian Sea

P. L'Hégaret et al.

Title Page

Abstract Introduction

Conclusions References

Tables Figures

◀ ▶

◀ ▶

Back Close

Full Screen / Esc

Printer-friendly Version

Interactive Discussion



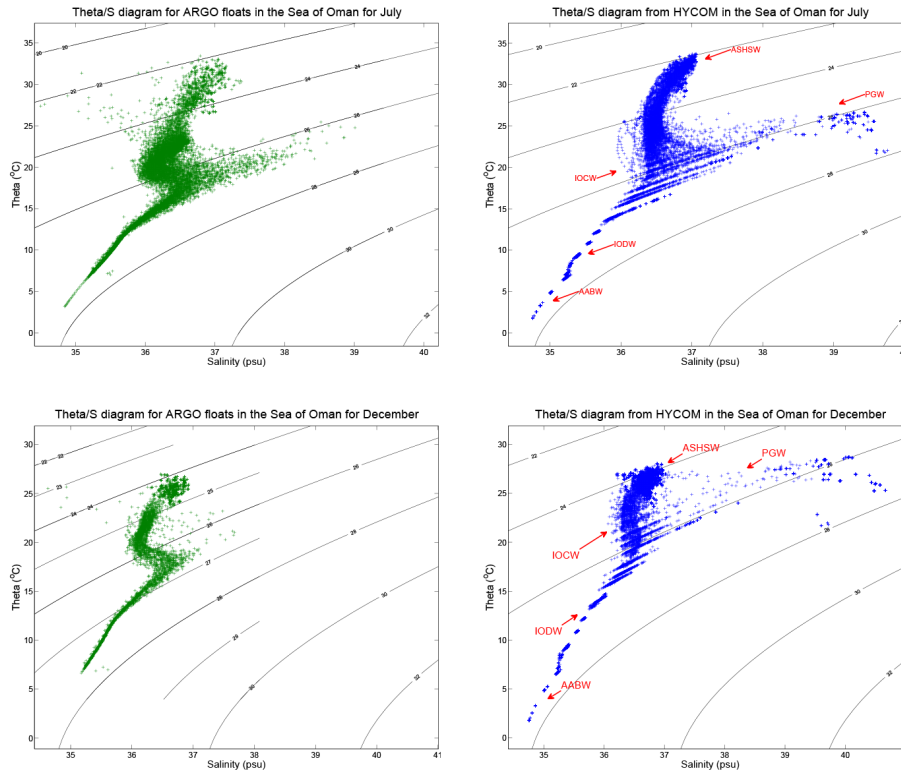


Figure 6. From top to bottom: potential temperature and salinity diagram for the Sea of Oman during July and December. On the left side, the diagram corresponds to the ARGO floats measurements; on the right side the values extracted from the HYCOM model. Abbreviations are: PGW: Persian Gulf Water; ASHSW: Arabian Sea High Salinity Water; IOCW: Indian Ocean Central Water; IODW: Indian Ocean Deep Water; AABW: Antarctic Bottom Water.

Title Page

Abstract Introduction

Conclusions References

Tables Figures

◀ ▶

◀ ▶

Back Close

Full Screen / Esc

Printer-friendly Version

Interactive Discussion



**Mesoscale variability
in the Arabian Sea**

P. L'Hégaret et al.

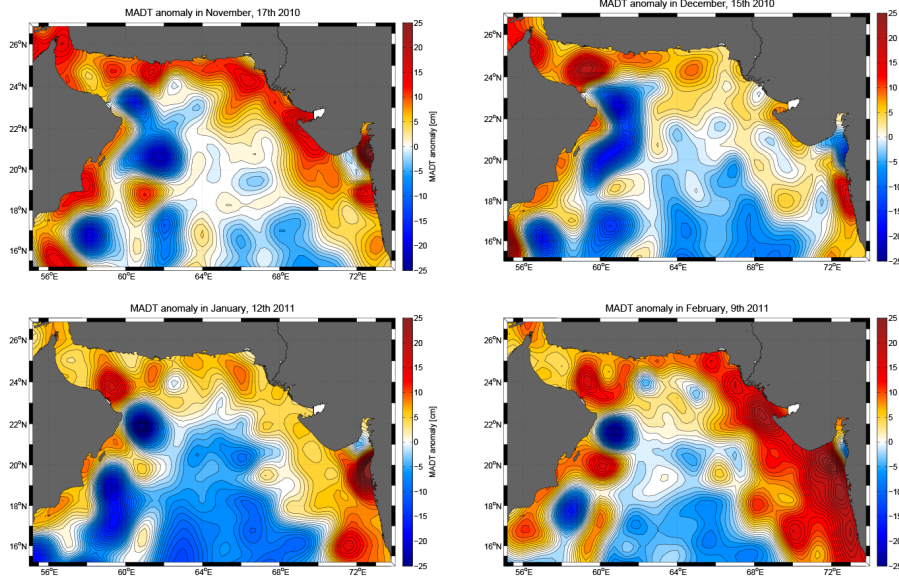


Figure 7. Evolution of the altimetry from November 2010 to February 2011, every 4 weeks.

Title Page	
Abstract	Introduction
Conclusions	References
Tables	Figures
◀	▶
◀	▶
Back	Close
Full Screen / Esc	
Printer-friendly Version	
Interactive Discussion	



**Mesoscale variability
in the Arabian Sea**

P. L'Hégaret et al.

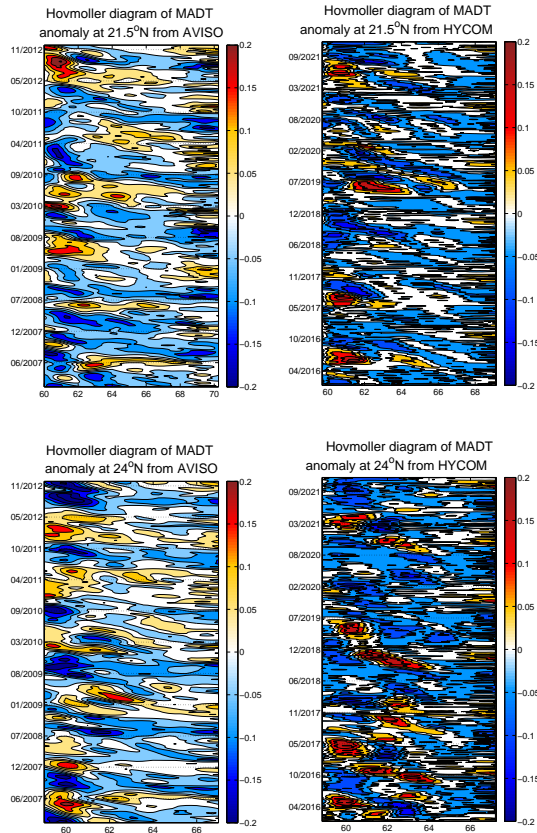


Figure 8. Hovmöller diagram over 6 years from AVISO (left) and HYCOM (right) at 21.5° N (top) and 24° N (bottom).

Title Page

Abstract Introduction

Conclusions References

Tables Figures

⏪ ⏩

◀ ▶

Back Close

Full Screen / Esc

Printer-friendly Version

Interactive Discussion



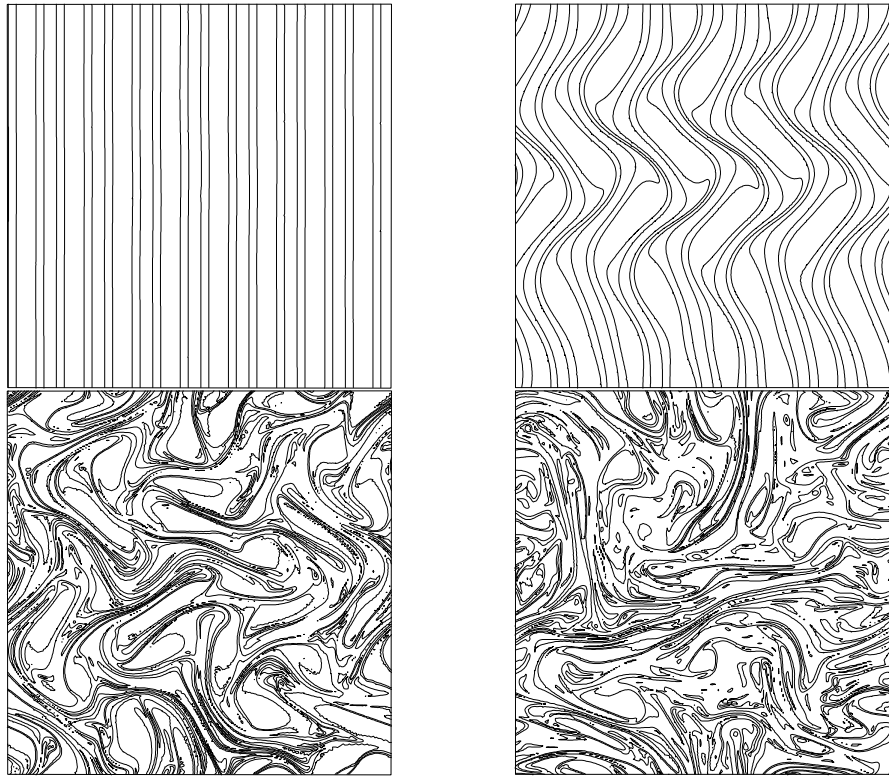


Figure 9. Panel of relative vorticity of a bi-dimensional incompressible flow. A Rossby waves ($\lambda = 180\text{km}$) crosses a sea mount (radius of 30 km) at the center of the simulated basin. Sub-plots are separated by a week interval. The maximum relative vorticity is $\xi_{RW} \approx 5 \times 10^{-5}$.

Mesoscale variability in the Arabian Sea

P. L'Hégaret et al.

Title Page	
Abstract	Introduction
Conclusions	References
Tables	Figures
◀	▶
◀	▶
Back	Close
Full Screen / Esc	
Printer-friendly Version	
Interactive Discussion	



Mesoscale variability in the Arabian Sea

P. L'Hégaret et al.

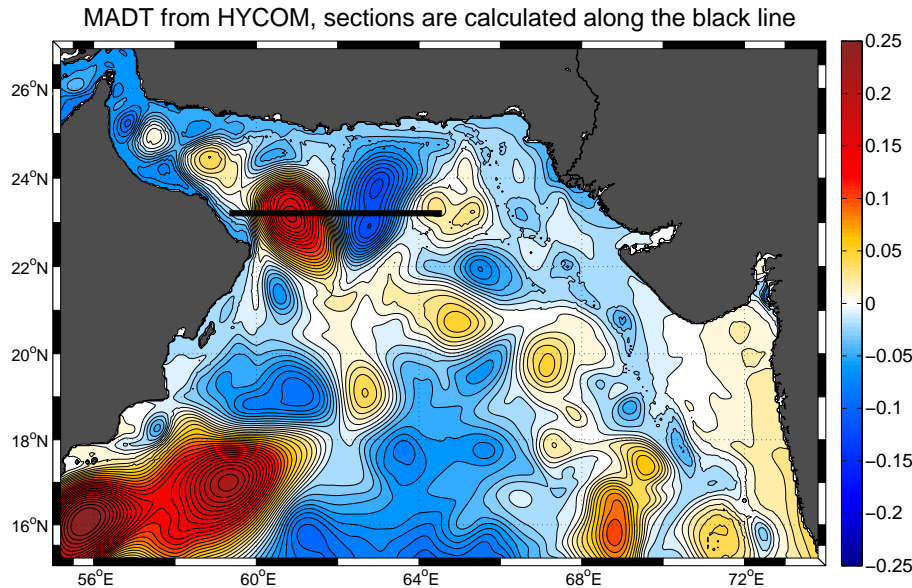


Figure 10. MADT anomaly map from HYCOM and position of the vertical section from West to East across an anticyclone and a cyclone during the spring intermonsoon season.

Title Page

Abstract

Introduction

Conclusions

References

Tables

Figures



Back

Close

Full Screen / Esc

Printer-friendly Version

Interactive Discussion



Mesoscale variability in the Arabian Sea

P. L'Hégaret et al.

Title Page

Abstract

Introduction

Conclusions

References

Tables

Figures

◀

▶

◀

▶

Back

Close

Full Screen / Esc

Printer-friendly Version

Interactive Discussion

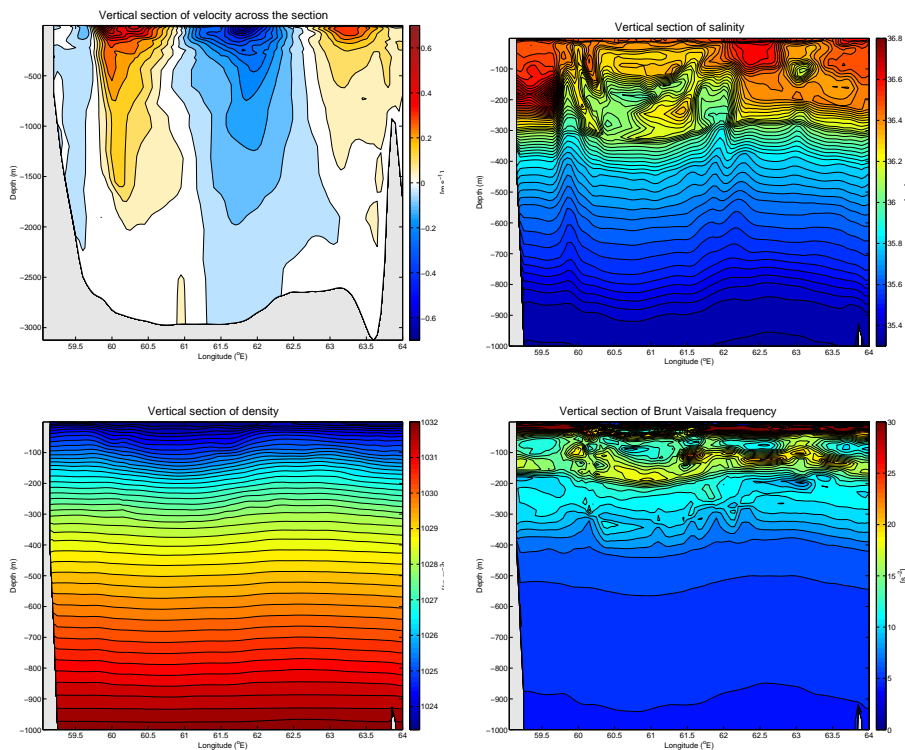


Figure 11. Vertical section from West to East across an anticyclone and a cyclone during the spring intermonsoon season; top left: velocity section (positive towards the North) down to 3000 m; top right: salinity section down to 1000 m; bottom left: density section down to 1200 m; bottom right: Brunt Väisälä frequency section.

**Mesoscale variability
in the Arabian Sea**

P. L'Hégaret et al.

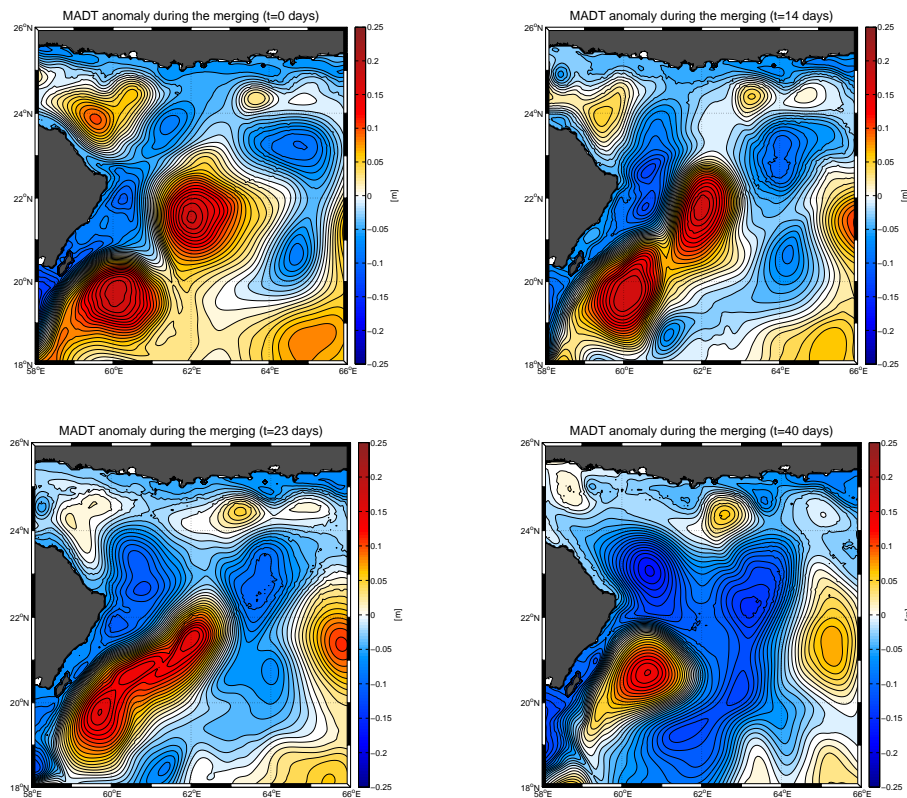


Figure 12. Evolution of the altimetry anomaly during a merger of two anticyclones for $t = 0$ (top, left), $t = 14$ days (top, right), $t = 23$ days (bottom, left) and $t = 44$ days (bottom, right).

Title Page

Abstract

Introduction

Conclusions

References

Tables

Figures

◀

▶

◀

▶

Back

Close

Full Screen / Esc

Printer-friendly Version

Interactive Discussion



Mesoscale variability in the Arabian Sea

P. L'Hégaret et al.

Title Page

Abstract

Introduction

Conclusions

References

Tables

Figures

◀

▶

◀

▶

Back

Close

Full Screen / Esc

Printer-friendly Version

Interactive Discussion

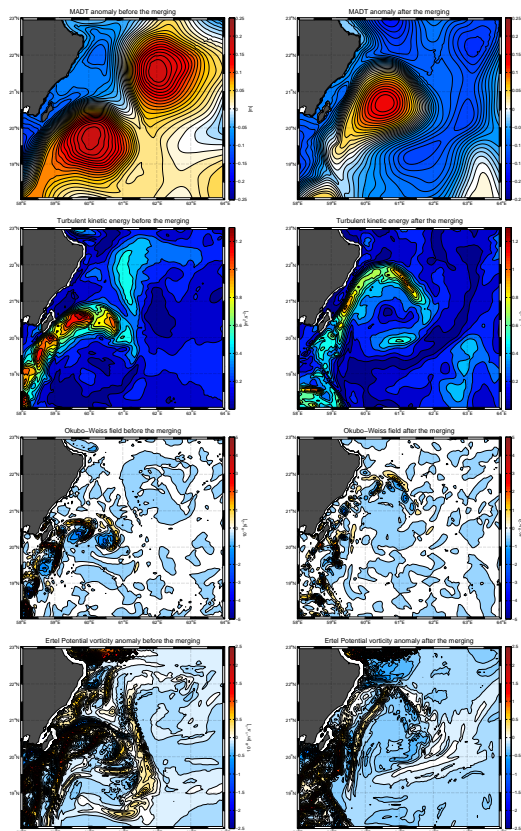


Figure 13. Fields before (left) and after (right) a merging of two anticyclonal eddies. First line: MADT anomaly maps; second line: turbulent kinetic energy; third line: Okubo–Weiss field (see text for computation) and fourth line: Ertel potential vorticity anomaly field (see text again). The northern PVE field is strongly positive due to a strong front of density in summer.

Mesoscale variability in the Arabian Sea

P. L'Hégaret et al.

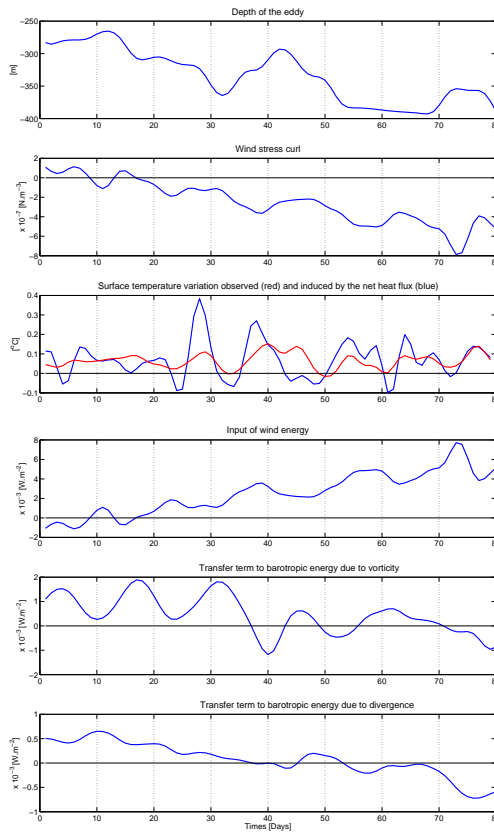


Figure 14. From top to bottom time series integrated over the surface of the eddy for: depth of the eddy (see text for computation), wind stress curl, variation of the sea surface temperature measured and induced by the net heat flux, wind work P_{Down} ; transfer term into barotropic energy due to vorticity $\{K' \bar{K}\}_{\zeta}$ and the transfer term due to divergence $\{K' \bar{K}\}_{\nabla}$.

Title Page

Abstract Introduction

Conclusions References

Tables Figures

◀ ▶

◀ ▶

Back Close

Full Screen / Esc

Printer-friendly Version

Interactive Discussion



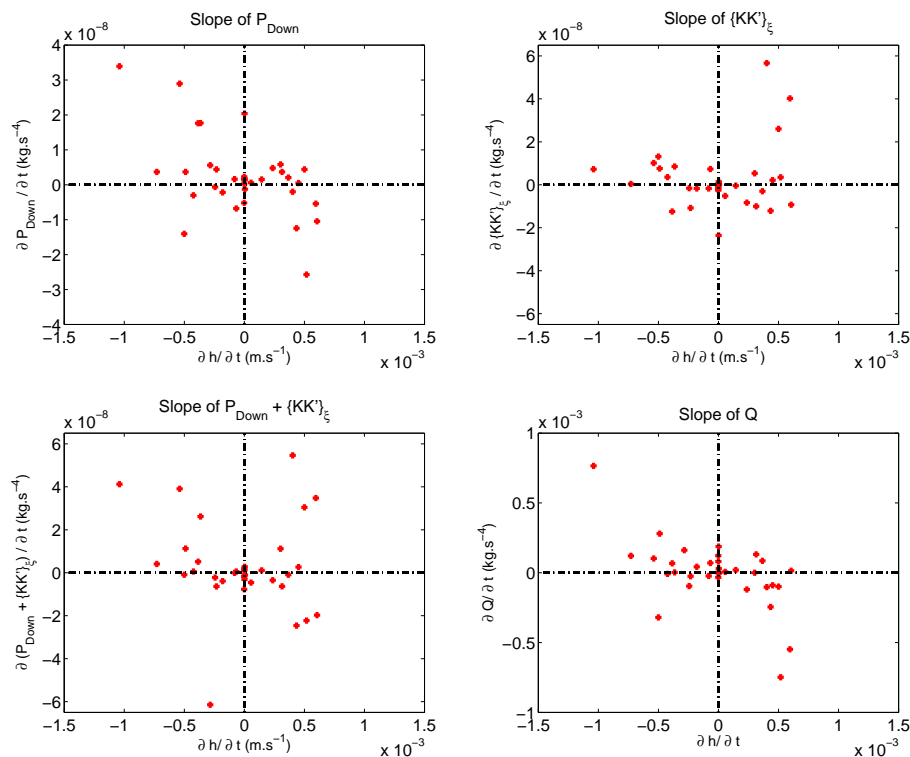


Figure 15. Comparison of the slope of transfer terms to the slope of the eddies depth. We followed 4 different eddies in spring for a total of 35 variations of depth. The parameters are the wind work P_{Down} (top, left); the transfer term from the baroclinic energy to barotropic due to vorticity $\{K'\bar{K}\}_{\xi}$ (top, right); the sum of those two (bottom, left) and the net heat flux (bottom, right).

Title Page

Abstract

Introduction

Conclusions

References

Tables

Figures



Back

Close

Full Screen / Esc

Printer-friendly Version

Interactive Discussion



**Mesoscale variability
in the Arabian Sea**

P. L'Hégaret et al.

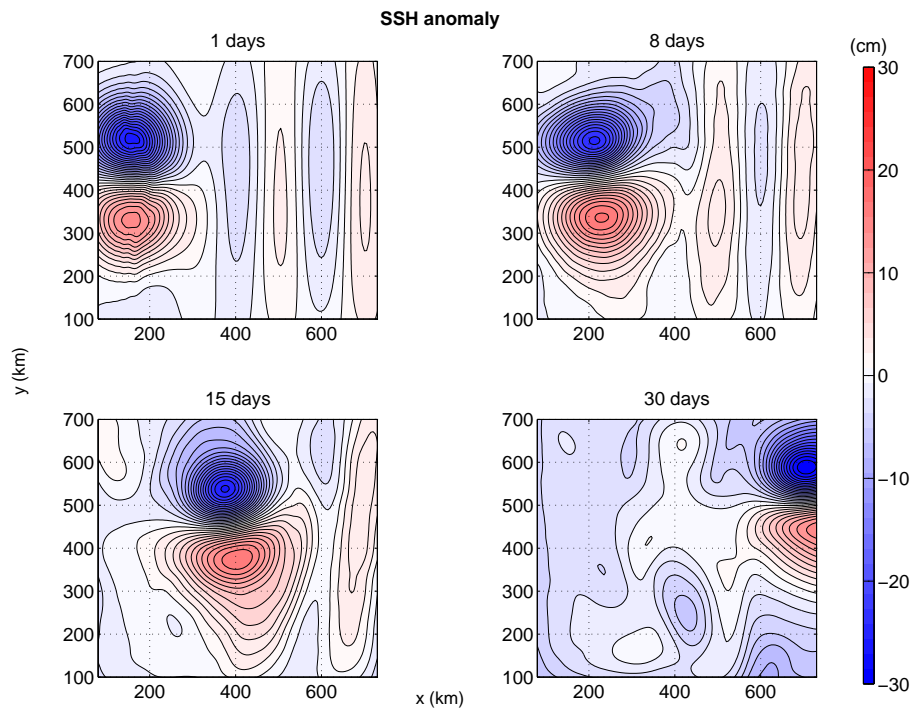


Figure 16. SSH fields. Evolution in time of the cyclone-anticyclone system and the Rossby wave train.



Mesoscale variability
in the Arabian Sea

P. L'Hégaret et al.

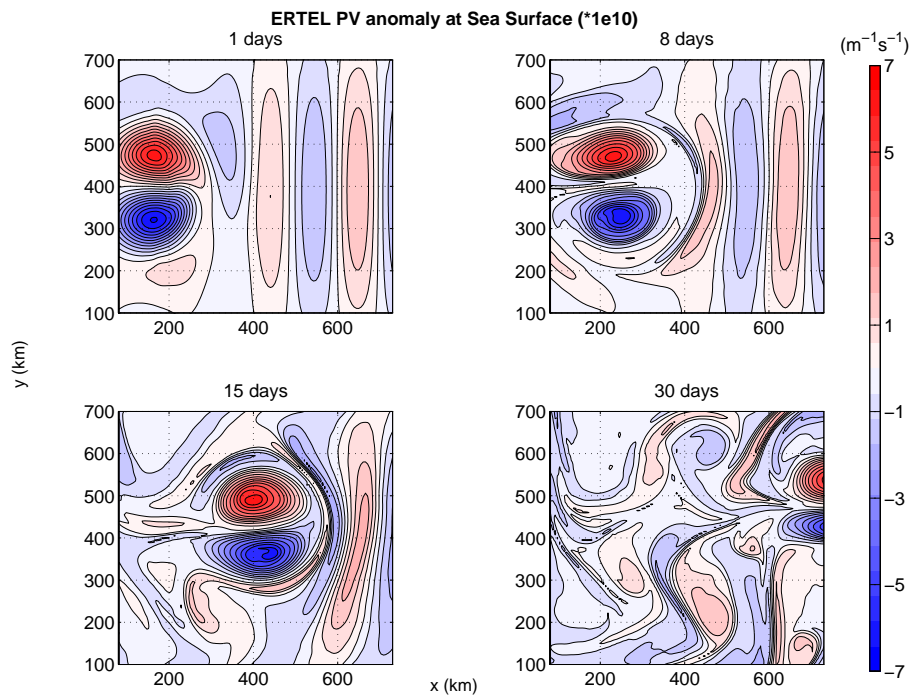


Figure 17. ERTel PV anomaly fields at the sea surface. Evolution in time of the cyclone-anticyclone system and the Rossby wave train.



**Mesoscale variability
in the Arabian Sea**

P. L'Hégaret et al.

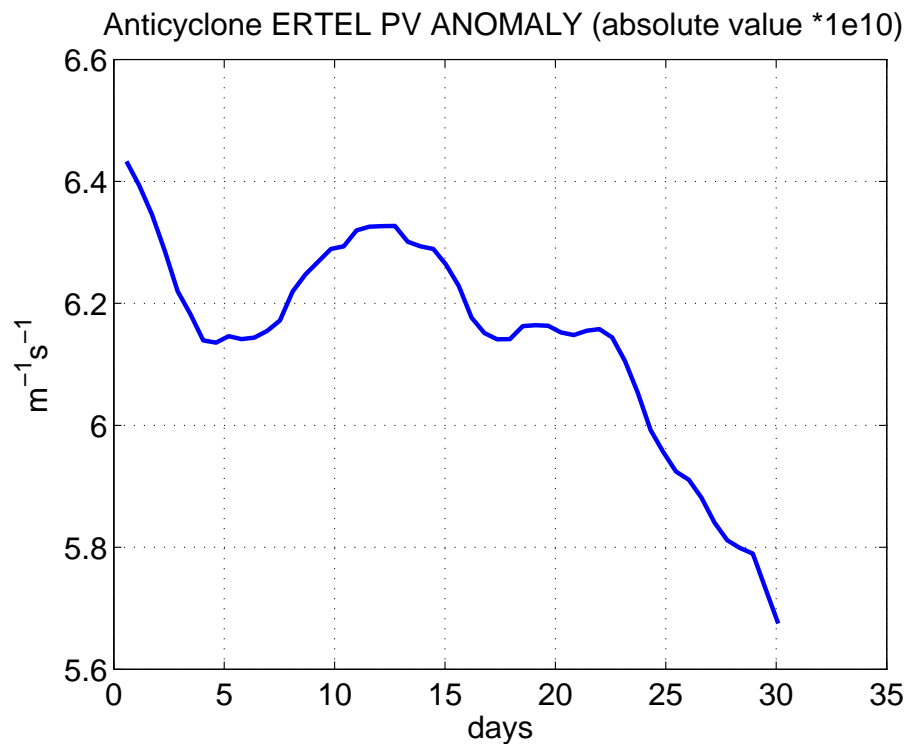


Figure 18. Modulus of ERTTEL PV anomaly for the anticyclonic eddy as a function of time.

[Title Page](#)[Abstract](#)[Introduction](#)[Conclusions](#)[References](#)[Tables](#)[Figures](#)[◀](#)[▶](#)[◀](#)[▶](#)[Back](#)[Close](#)[Full Screen / Esc](#)[Printer-friendly Version](#)[Interactive Discussion](#)

**Mesoscale variability
in the Arabian Sea**

P. L'Hégaret et al.

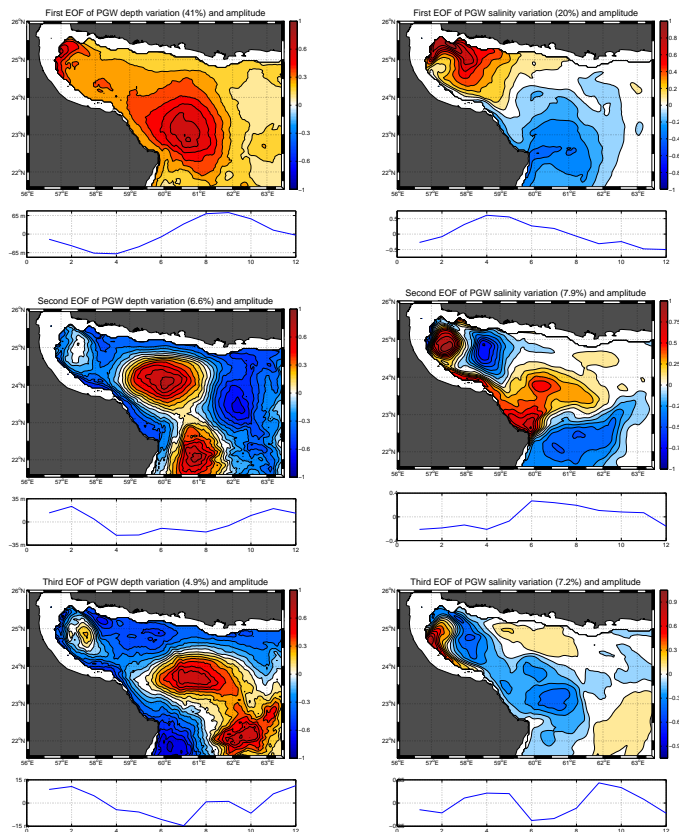


Figure 19. First three EOF's of PGW depth anomaly (left) and salinity anomaly (right), computed with HYCOM for 4 years.

[Title Page](#)[Abstract](#)[Introduction](#)[Conclusions](#)[References](#)[Tables](#)[Figures](#)[◀](#)[▶](#)[◀](#)[▶](#)[Back](#)[Close](#)[Full Screen / Esc](#)[Printer-friendly Version](#)[Interactive Discussion](#)

**Mesoscale variability
in the Arabian Sea**

P. L'Hégaret et al.

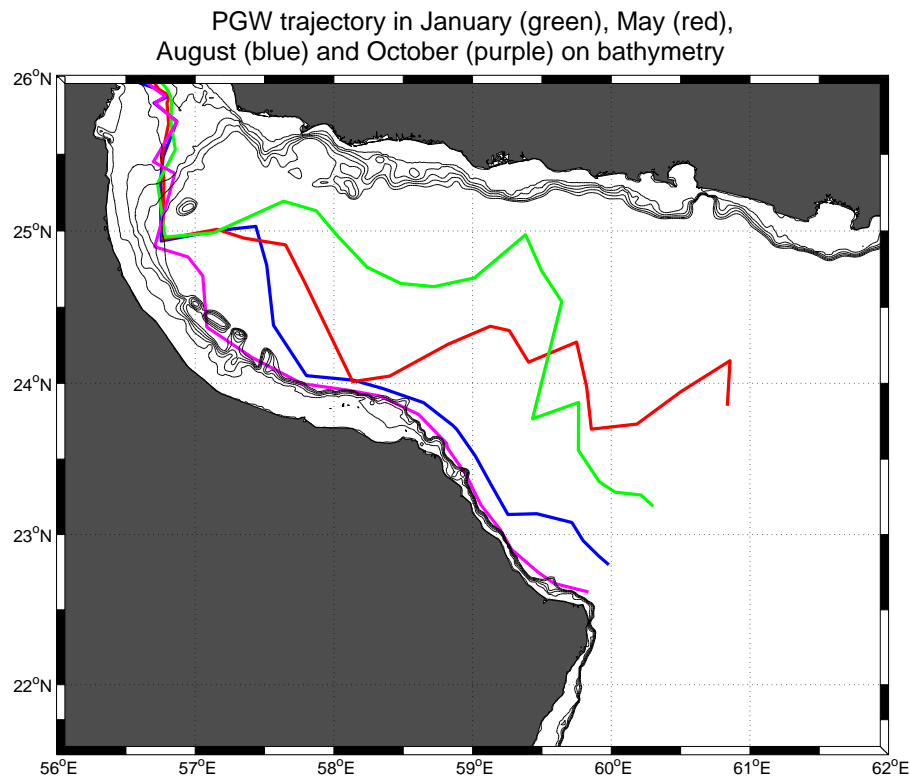


Figure 20. Trajectory of the PGW maximum, extracted from HYCOM, for 4 months characteristic of each seasons, superimposed on bathymetry line from 0 to 250 m, each 50 m.

[Title Page](#)[Abstract](#)[Introduction](#)[Conclusions](#)[References](#)[Tables](#)[Figures](#)[◀](#)[▶](#)[◀](#)[▶](#)[Back](#)[Close](#)[Full Screen / Esc](#)[Printer-friendly Version](#)[Interactive Discussion](#)

Mesoscale variability in the Arabian Sea

P. L'Hégaret et al.

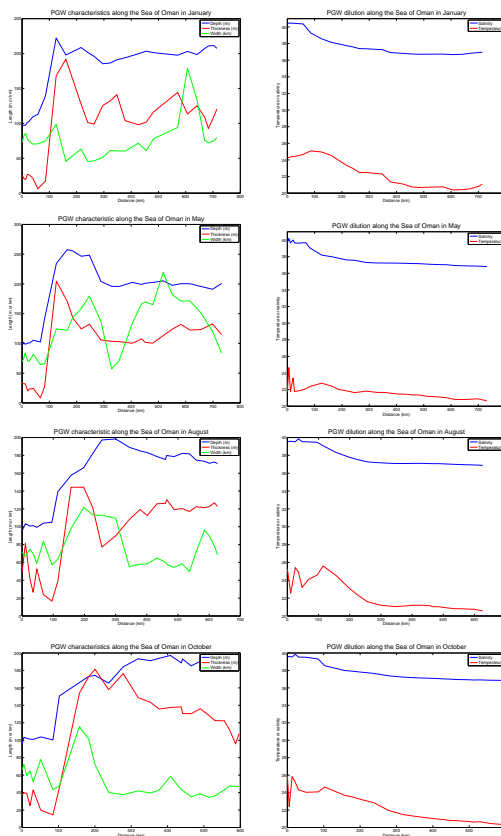


Figure 21. Characteristics (left) and dilution (right), of the PGW for each seasons along their respective trajectories, described in Fig. 20.

[Title Page](#)
[Abstract](#)
[Introduction](#)
[Conclusions](#)
[References](#)
[Tables](#)
[Figures](#)

[Back](#)
[Close](#)
[Full Screen / Esc](#)
[Printer-friendly Version](#)
[Interactive Discussion](#)


**Mesoscale variability
in the Arabian Sea**

P. L'Hégaret et al.

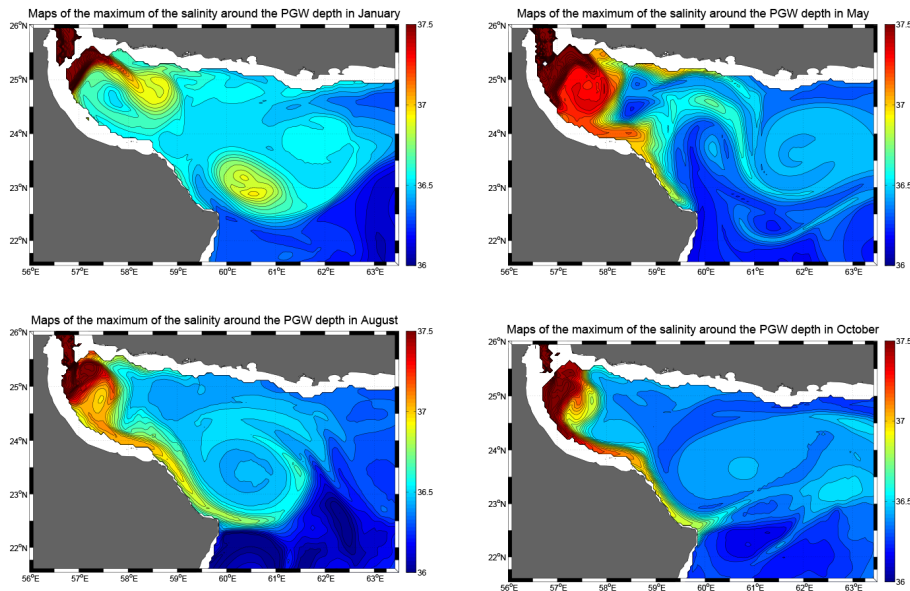


Figure 22. Salinity maps of the maximum of salinity around the PGW depth for 4 months characteristics of each seasons.

[Title Page](#)[Abstract](#)[Introduction](#)[Conclusions](#)[References](#)[Tables](#)[Figures](#)[◀](#)[▶](#)[◀](#)[▶](#)[Back](#)[Close](#)[Full Screen / Esc](#)[Printer-friendly Version](#)[Interactive Discussion](#)

**Mesoscale variability
in the Arabian Sea**

P. L'Hégaret et al.

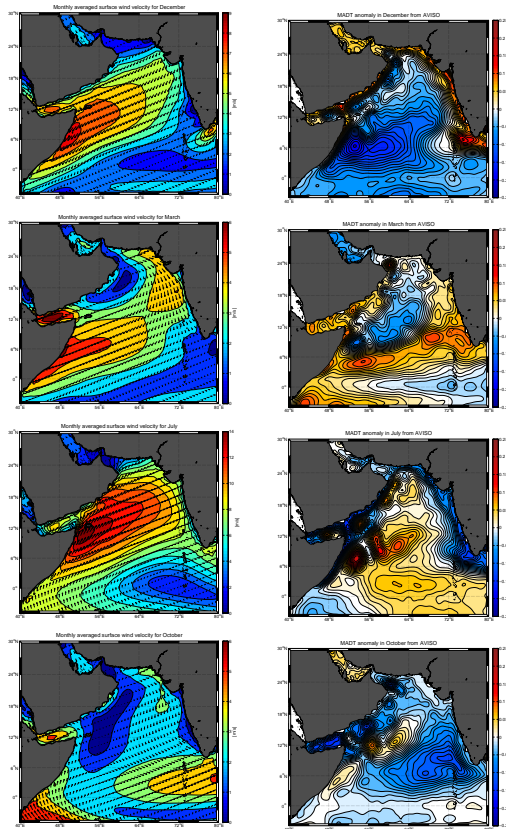


Figure 23. Fields of monthly averaged wind intensities and orientation (left) and MADT anomaly from AVISO (right) in December, March, July and October (from top to bottom).

Title Page

Abstract

Introduction

Conclusions

References

Tables

Figures



Back

Close

Full Screen / Esc

Printer-friendly Version

Interactive Discussion



**Mesoscale variability
in the Arabian Sea**

P. L'Hégaret et al.

Title Page

Abstract

Introduction

Conclusions

References

Tables

Figures



Back

Close

Full Screen / Esc

Printer-friendly Version

Interactive Discussion

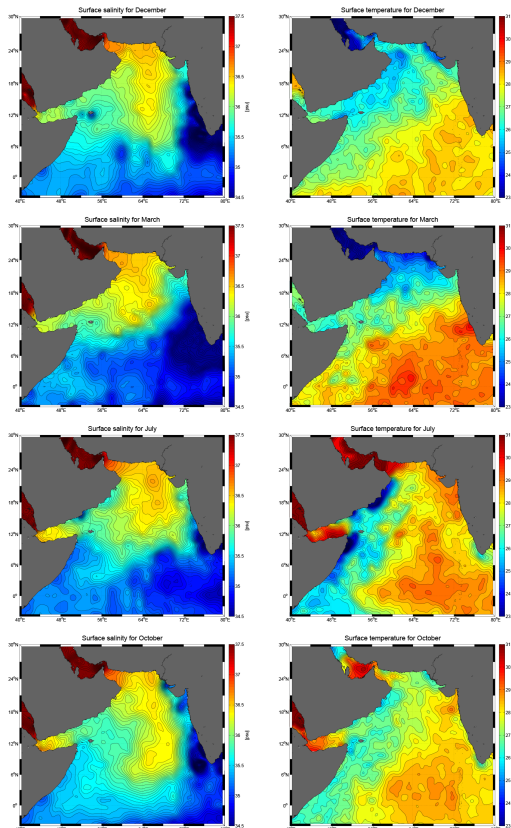


Figure 24. Fields of climatological surface salinity (left) and surface temperature (right) in December, March, July and October (from top to bottom).

**Mesoscale variability
in the Arabian Sea**

P. L'Hégaret et al.

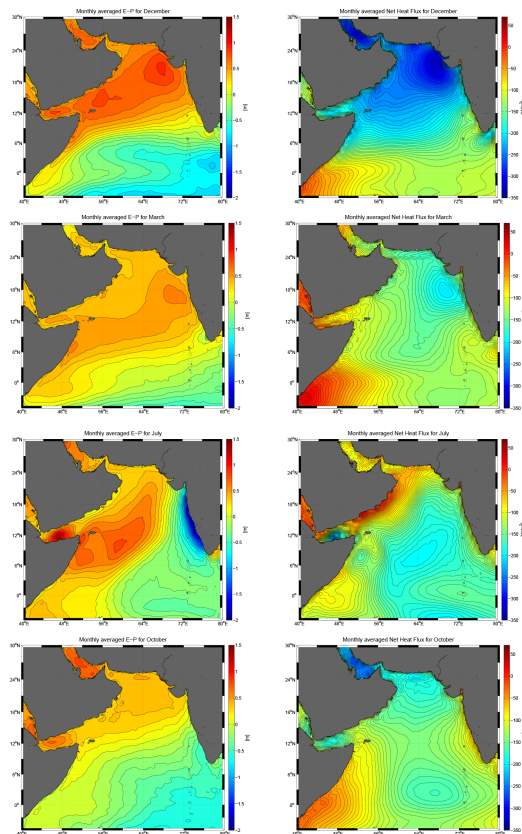


Figure 25. Fields of monthly averaged Evaporation/Precipitation budget (left) and net heat flux (right) in December, March, July and October (from top to bottom).

[Title Page](#)[Abstract](#)[Introduction](#)[Conclusions](#)[References](#)[Tables](#)[Figures](#)[◀](#)[▶](#)[◀](#)[▶](#)[Back](#)[Close](#)[Full Screen / Esc](#)[Printer-friendly Version](#)[Interactive Discussion](#)